Research Article

New paleohydroclimate record of the MIS 5e/5d transition from Yelini Cave, central Anatolian region of Türkiye

Kaan Gürbüz[a], Halim Mutlu[a], Ezgi Ünal-İmer[b]* , İ. Tonguç Uysal[c,d] and Jian-Xin Zhao[d]

[a]Department of Geological Engineering, Ankara University, 06830 Gölbaşı, Ankara, Türkiye; [b]Department of Geological Engineering, Middle East Technical University, 06800 Çankaya, Ankara, Türkiye; [c]Department of Geological Engineering, İstanbul Cerrahpaşa University, 34320 Avcılar, Türkiye and [d]School of the Environment, The University of Queensland, Brisbane St Lucia, QLD 4072, Australia

Abstract

This study presents the results of a detailed paleoclimate investigation on stalagmite YL-1 (Yelini Cave, Türkiye). YL-1 grew between 117.13 (+0.57/−0.44) ka and 114.87 (+1.63/−2.89) ka within Greenland Stadial 26, indicating a positive moisture balance during the stadial conditions in this semi-arid region. Rainfall is significantly affected by sub-cloud and surface evaporation and decreasing net effective winter precipitation is recorded by high isotope values. Enriched $\delta^{18}O$ and $\delta^{13}C$ at 116.65 (+0.51/−0.39) ka are interpreted as a drought event that took place ca. 400 years before the end of the MIS 5e. This event, which was reported simultaneously in marine and terrestrial archives in the Northern Hemisphere, is a result of decreased cyclone activity linked to weakening of the Atlantic meridional overturning circulation. $^{87}Sr/^{86}Sr$ values of YL-1 are close to the host-rock values. Decreased $^{87}Sr/^{86}Sr$ ratio at 116.67 (+0.54/−0.38) ka reflects the intensified water–rock interaction due to lower precipitation. Along with prior calcite precipitation effect, this is also observed by increased Mg/Ca and Sr/Ca, while low P, Cu, Be, Y, and Zr concentrations indicate a lowered amount of soil-derived colloidal material. The MIS 5e/5d transition is marked by reduced insolation and enriched $\delta^{18}O$ at 116.24 (+0.53/−0.86) ka. The Greenland Interstadial 25 phase at 115.87 (+0.83/−1.71) ka is represented by more negative $\delta^{18}O$ and $\delta^{13}C$.

Keywords: Interglacial, Paleoclimate, Speleothem, Stable isotope, Trace element, Sr isotope, Central Türkiye

INTRODUCTION

Glacial–interglacial transitions provide precise archives for climate events. This is due to the influence of orbital parameters on the timing of events occurring in these intervals, as well as due to the expansion of the ice sheets and its effect on the oceans and moisture balance. Marine Isotope Stage (MIS) 5 interval (ca. 130–74 ka) is represented by the last interglacial period (LIG) and the onset of the last glacial (Capron et al., 2010). The MIS 5e substage covers the interval of 130–116 ka (130 through ca. 120 ka in the eastern Mediterranean [EM] and eastern Europe based on terrestrial archives [Demény et al., 2017]), during which the sea level is estimated to have been 6–9 m higher than the current global average (Kukla et al., 2002; Shackleton et al., 2003; Dutton et al., 2015). The LIG and following glacial inception periods are climatically important periods since they have the potential to allow us to reconstruct the possible responses to climatic variations triggered by current global warming (Govin et al., 2015).

The continuous ca. 123 ka-long $\delta^{18}O$ record of the North Greenland Ice Core Project (NGRIP) ice core is very valuable because it also includes a part of the LIG period (NGRIP members, 2004). High temperatures during the LIG are represented by high values of $\delta^{18}O$ (−32‰) (NGRIP members, 2004). During the LIG, the Mediterranean woody taxa reached its highest abundance (Brauer et al., 2007). Later, this warm interval was interrupted by glacial expansion and some cold-water events in the North Atlantic (Kukla et al., 2002). The NGRIP records indicate a gradual depletion of $\delta^{18}O$ towards 116 ka with a transition to cold conditions. The end of the cooling phase is defined as the Greenland Stadial 26 (GS 26) interval, which marks the MIS 5e/5d transition.

A cooling of 4°C is suggested to have occurred between the C25 cold-water event and the last interglacial optimum (Oppo et al., 2006). In addition, the planktonic $\delta^{18}O$ record indicates the C26 cold-water event during early ice sheet growth, pointing to a 2–3°C decrease in North Atlantic sea surface temperature (Chapman and Shackleton, 1999) and the warm period of MIS 5e lasting ca. 9–10 ka that gradually ended with the C26 and C25 cold-water events (Oppo et al., 2006). The C25 cooling event associated with the end of GS 26 also indicates a decrease in woody taxa, pointing towards a decrease in moisture availability in the eastern Anatolian pollen records (Pickarski et al., 2015). Proxies of the LIG and the beginning of the glacial period have been discussed in detail using glacial (Johnsen et al., 1997; NGRIP members, 2004), marine (McManus et al., 1994; Fronval and Jansen, 1997; Chapman and Shackleton, 1999;

Sánchez Goñi et al., 1999, 2012; Oppo et al., 2001, 2006; Knudsen et al., 2002; Melki et al., 2010; Galaasen et al., 2014; Irvali et al., 2016), and speleothem records of the North Atlantic and European regions (Drysdale et al., 2005, 2007, 2009; Boch et al., 2011; Moseley et al., 2015; Vansteenberge et al., 2016, 2019; Dumitru et al., 2018; Nicholson et al., 2021). The effects of climatic changes in the eastern Mediterranean occurring in both the last interglacial and glacial inception periods have been reported in several studies (e.g., Bar-Matthews et al., 2003; Nehme et al., 2015; Columbu et al., 2019), but are not fully known in Türkiye. For this reason, it is important to investigate the potential effects of sub-millennial climate changes during the last interglacial–glacial inception on the Anatolian Peninsula.

Due to its geographic setting, Türkiye is affected by various climatic domains (e.g., Atlantic, Mediterranean, and Asian; Rowe et al., 2012). Regional climate is dominated mainly by humid and cold air masses originating from the north and northwest, as well as by mid-latitude subtropical anticyclones (Akçar and Schlüchter, 2005; Türkeş, 2020). The high-pressure systems initiating from Siberia, which are cold and dry in winter, and the extensions of the low-pressure monsoon system originating from Asia in summer are other climate systems affecting the region (Akçar and Schlüchter, 2005; Türkeş, 2020; Jacobson et al., 2022). Precipitation in the region is mainly controlled by the North Atlantic Oscillation (NAO) (Türkeş, 2020). While strong precipitation conditions are observed in winter and autumn months in Türkiye during the NAO negative phase, weaker precipitation conditions prevail during the positive phases (Türkeş and Erlat, 2003, 2005). Therefore, considering its effect on winter precipitation, the Anatolian Peninsula is extremely important in order to explore the eastern extensions of climatic changes in the last glacial inception period.

Stalagmites (secondary cave carbonates) can physically and chemically record climatic and environmental events during the time of their formation in isotopic equilibrium with the dripping water (McDermott et al., 2006). Precise dating of these deposits up to 600,000 years using the U-series dating technique (White, 2004) has played an important role in establishing long-term terrestrial climate records. The chronological records of the LIG are generally based on the alignment (correlation) technique of various proxies, which may lead to some discrepancies in ages. High-precision age data obtained from speleothems, however, can provide good age-calibrated climate records (Govin et al., 2015).

Speleothem-based paleoclimate studies in Türkiye are mostly focused on the last ice age or the Holocene period, some with important linkages with early human settlements (Fleitmann et al., 2009; Göktürk et al., 2011; Rowe et al., 2012; Ünal-İmer et al., 2015, 2016a; Koç et al., 2020; Erkan et al., 2021; Jacobson et al., 2021, 2022). The oldest records from the region are from Sofular (Badertscher et al., 2011) in NW Türkiye and Dim Cave (Rowe et al., 2020) from SSW Türkiye. The study on Dim Cave (Alanya) by Rowe et al. (2020) focused on the beginning of the last interglacial period, but the climate record does not extend into the last interglacial–glacial transition. In addition, the Sofular Cave record characterizes different climatic conditions that do not reflect true Mediterranean climate due to significant humidity over the Black Sea. There is a lack of speleothem-based record of the last glacial inception in Türkiye. This study fills this gap by presenting new stable and radiogenic isotope (δ^{13}C and δ^{18}O, ^{87}Sr/^{86}Sr) and trace element (Ca, Mg, Sr, P, Cu, Y, Be,

and Zr) data from a MIS 5 stalagmite (YL-1) collected from Yelini Cave (Fig. 1) and provides the first multi-proxy climate record of the MIS 5e/5d transition from the central Anatolia.

REGIONAL CHARACTERISTICS

Yelini Cave

The Yelini Cave (also known as the Yılanlı Cave) is located near the town of Kayakent in the Günyüzü district of Eskişehir Province in central Türkiye. The cave is accessed through a narrow entrance along the southwest side of the Sivrihisar Mountains (Fig. 1). Yelini has archaeological importance because artifacts there include remains and cave paintings suggesting prolonged periods of human use in Neolithic times (Nazik et al., 2001).

Yelini Cave (39°14'23.28"N, 31°48'25.33"E) (Fig. 1), located at an altitude of 1105 m above sea level (asl), is a horizontally extending fossil cave with a total length of 271 m (Nazik et al., 2001) (Fig. 1b). Yelini Cave is dry except for the drip waters seeping from the ceilings during wet seasons (Nazik et al., 2001) through a thin cover of limestone in the region. Its deepest point lies ~26 meters below the cave entrance. Relative humidity within the cave varies from 45% in the entrance to 79% in the deepest gallery where the YL-1 stalagmite was collected in 2019 (Fig. 1).

Geology

Yelini Cave lies within the Günyüzü Basin, which is a sub-basin of the Sakarya Basin (Demiroğlu and Örgün, 2010). Exposed lithologies include Paleozoic metamorphic rocks (Sivrihisar Metamorphics), Miocene sedimentary rocks, and Quaternary cover units (mainly alluvium) (Demiroğlu, 2008) (Fig. 1). The cave itself formed within Paleozoic marbles, which have been intensely karstified and have been significantly affected by a NW–SE-trending fault (Fig. 1a; Nazik et al., 2001; Şenoğlu, 2006; Demiroğlu, 2008).

Climate

The modern climate of the Anatolian Peninsula is heterogeneous. Located in the middle latitude temperate zone, Türkiye experiences four seasons throughout the year due to its close proximity to the sub-tropical zone (Türkeş, 2020). While the coastal regions are represented by a Mediterranean climate, the inland Anatolian Plateau experiences a continental climate (Bozkurt and Şen, 2009). Mountain belts extending parallel to the coast in the southern and northern regions prevent the marine climate from reaching the inner regions (Ünal et al., 2012). Therefore, precipitation received by the coastal regions is significantly higher than in the inner high plateaus of central Anatolia and the transportation of moisture to the interior is provided through the E–W trending valleys between the mountain ranges extending perpendicular to the Aegean coast in the western part of Anatolia (Bozkurt and Şen, 2009). Because of these topographical barriers, the central Anatolian region, where the Yelini Cave is situated, has semi-arid climate conditions (Altın et al., 2012). For this reason, winters are cold and rainy, spring months are cool and rainy, and summers are mildly rainy (Türkeş, 2003). According to data from the Turkish General Directorate of Meteorology for the year 2020, the average annual temperature of the Eskişehir region is 11°C,
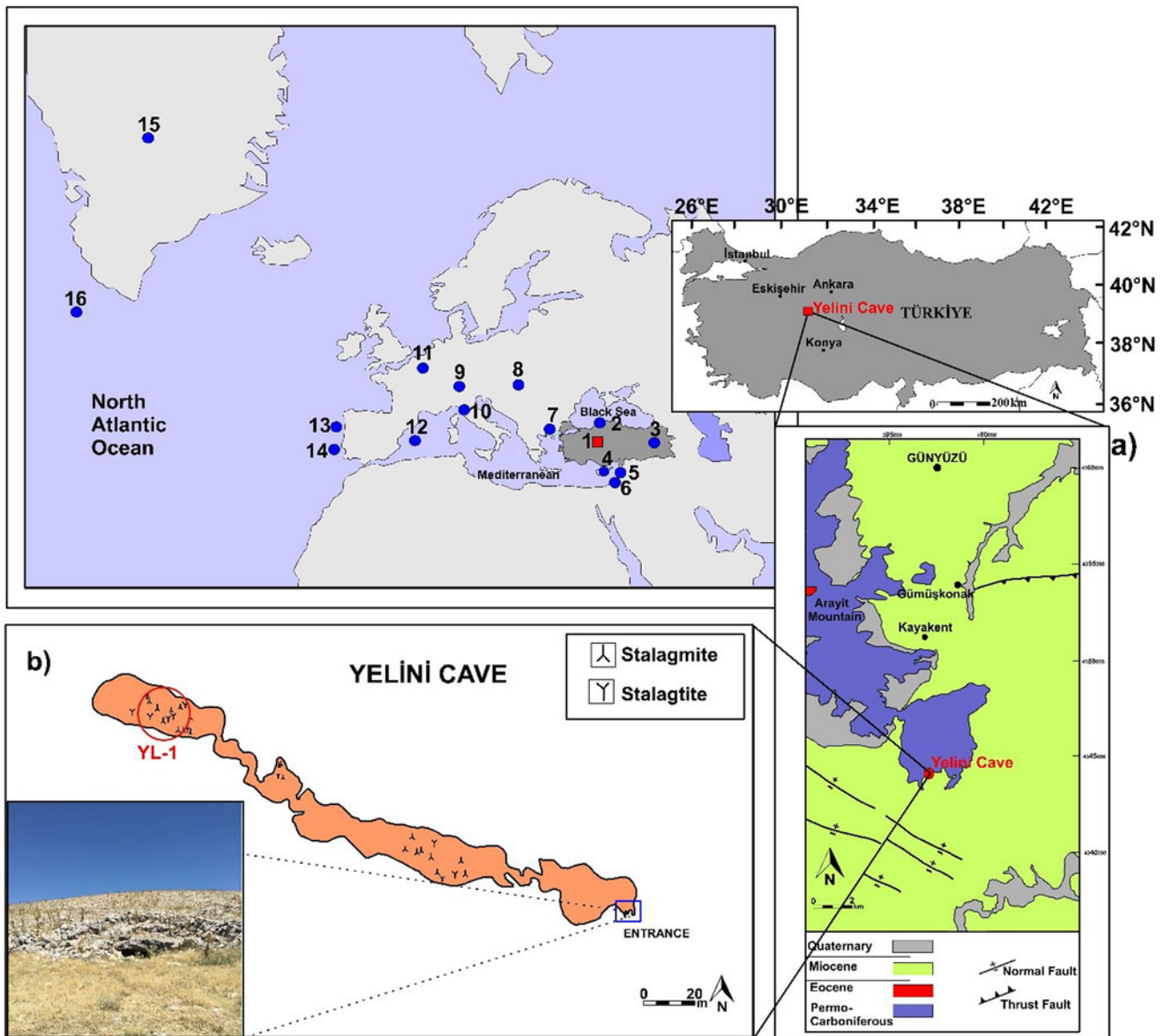
Figure 1. Locations of the records: 1 – Yelini Cave (Türkiye); 2 – Sofular Cave (Türkiye); 3 – Van Lake (Türkiye); 4 – Pentadactylos Cave (Cyprus); 5 – Kanaan Cave (Lebanon); 6 – Soreq and Peqiin caves (Israel); 7 – Tenaghi-Phillippon (Greece); 8 – Baradla Cave (Hungary); 9 – Schneckenloch and Hölloch caves (Austria and Switzerland); 10 – Corchia Cave (Italy); 11 – Han-Sur-Lesse Cave (Belgium); 12 – Campanet Cave (Mallorca); 13 – MD95-2040 core (Iberian margin); 14 – MD01-2443 core (Iberian margin); 15 – North Greenland Ice Core Project (NGRIP); 16 – MD03-2664 core (Labrador Basin). (a) Location and geological map of the study area (modified from Demıroğlu, 2008). (b) Map of the Yelini Cave (modified from Nazik et al., 2001).

and the average annual precipitation is 365 mm. The highest precipitation occurs in January, March, May, and June, while lowest precipitation is recorded in July and November (Fig. 2). Potential evapotranspiration exceeds precipitation in average conditions throughout the year (Türkeş, 2020).

The predominance of winter precipitation in the region reflects the annual NAO effect. The dominant influence of NAO on Europe and the Mediterranean basin is particularly important in terms of received precipitation in western and central parts of Anatolia (Türkeş and Erlat, 2003). In the negative phase of NAO, weakening of Azores high pressure and shifting of maritime polar air masses to a southward route and evaporation over the western Mediterranean increase the extent of rainy conditions (Bozkurt and Şen, 2009).

MATERIAL AND METHODS

Sample description

The YL-1 stalagmite was collected from the interior of the cave far from the entrance in an area with limited ventilation (Fig. 1b). The total length of the stalagmite is 14.1 cm, and due to the absence of laminae and textural evidence for possible secondary crystallization and deformation, the upper 0.9 cm section was not studied (Fig. 3).

The laminae are quite prominent along the stalagmite growth. Thinly developed laminae (1 mm thickness or less) of the sample are generally light brown, cream, beige, and white in color. A dark-brown layer is observed at 7.7–8.0 cm from the apex, which divides the stalagmite into two distinct growth periods
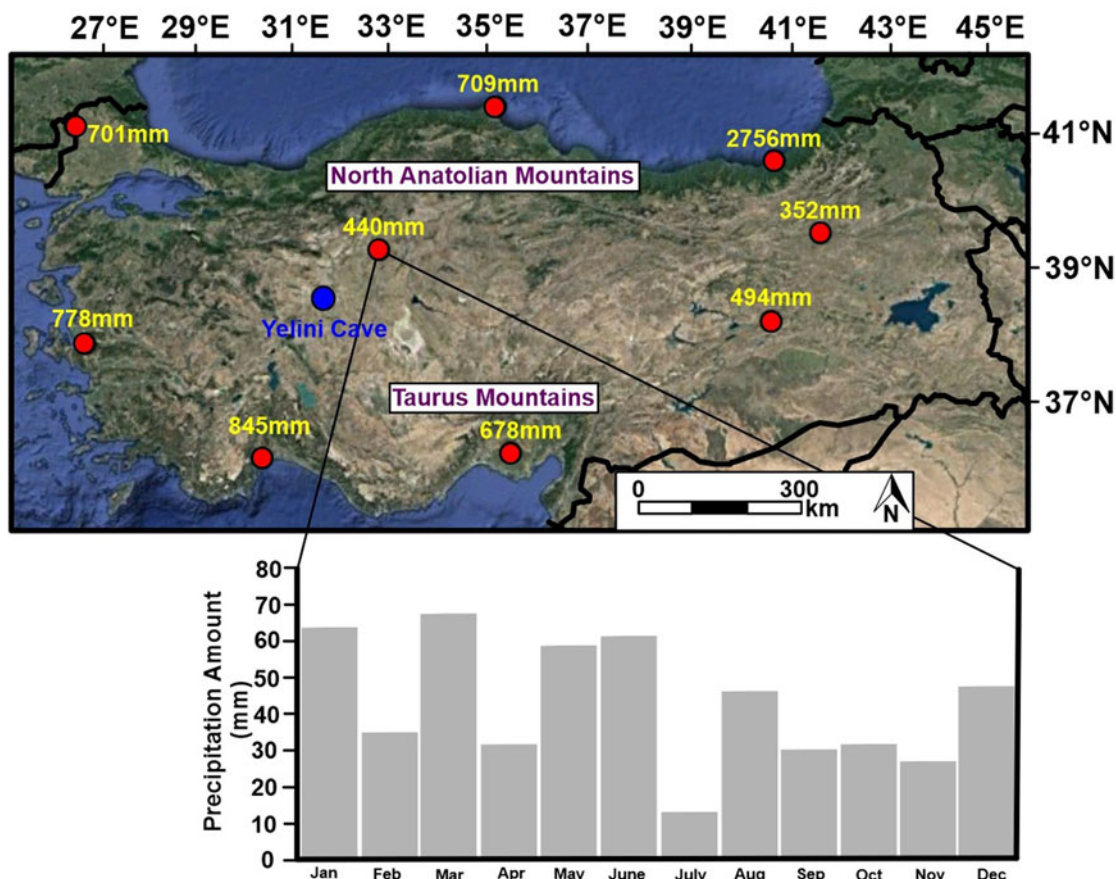
Figure 2. The distribution of yearly regional rainfall in Türkiye (5-year average values during 2012–2016; Dilaver et al., 2018).

(Fig. 3). Changing of growth axes is evident for these growth periods. The lower and upper axes are 5.0 and 7.5 cm long, respectively (Fig. 3). The width of the YL-1 stalagmite is ∼6 cm, but there are minor variations in thickness.

Mineralogy

Thin-section petrography and XRD studies were carried out for mineralogical investigations. Three thin sections were prepared from one-half of the YL-1 stalagmite at the Ankara University
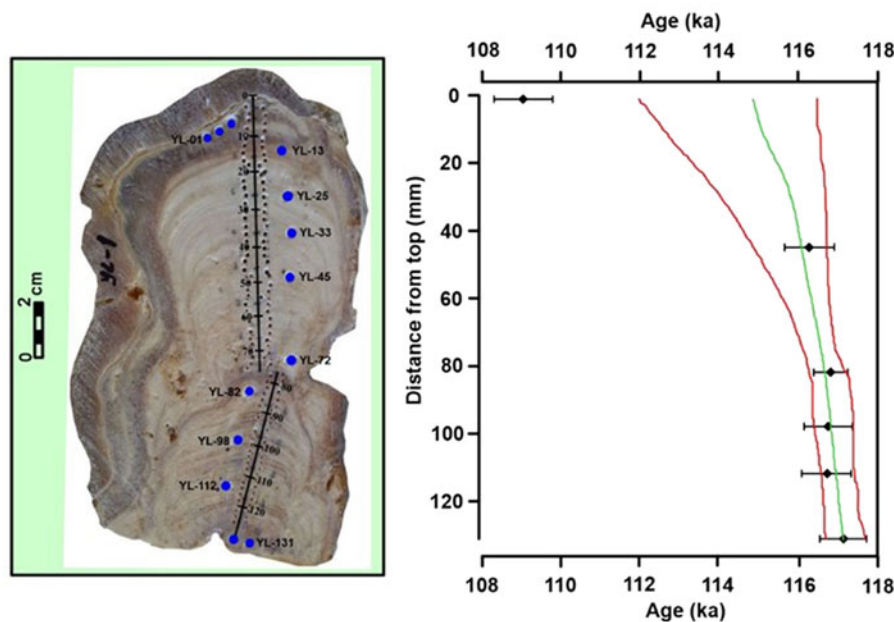

Figure 3. Photograph of the YL-1 stalagmite half showing the growth axes and locations of samples dated by U-series (left). Age–depth model generated on StalAge (Scholz and Hoffmann, 2011; Scholz et al., 2012) using U-series ages of sub-samples at distances of 1, 45, 82, 98, 112, and 131 mm (right). Red lines indicate the age error boundaries.

Earth Sciences Application and Research Center (YEBİM) and textural changes of the laminae were examined under a polarizing microscope.

XRD analyzes were performed on laminae from which age data were obtained. The analyses were carried out with the Panalytic-Aeris device in YEBİM by selecting ∼500 mg of powder sample for each.

U-Series dating

The U-series dating method was used for dating of the YL-1 stalagmite. Ten sub-samples, each weighing 100–150 mg, were collected from the stalagmite (Fig. 3). Microsampling was performed at the points of 1, 13, 25, 33, 45, 72, 82, 98, 112, and 131 mm from the top of the stalagmite. Sampling was carried out as much as possible from the impurity-free parts of the calcite layers. Drill bits used for microdrilling were cleaned with distilled water and ethyl alcohol after each sampling.

U-Series dating of the samples was performed at the University of Queensland (Australia) Radiogenic Isotope Laboratory (School of the Environment) using the Nu Plasma HR Multi-collector Inductively Coupled Plasma Mass Spectrometer (MC-ICP-MS). The analysis was carried out using the analytical protocols described by Zhao et al. (2001) and Ünal-İmer et al. (2015), and the results are reported in Table 1.

Stable isotope analysis

For carbon and oxygen isotopic analyses, 127 calcite sub-samples were collected from the stalagmite at 1 mm intervals using an micro hand drill. In addition, one marble wall-rock sample was also analyzed for its carbon and oxygen isotope composition.

Carbon and oxygen isotope analyses were performed at the Environmental Isotope Laboratory of the University of Arizona (USA). $\delta^{18}O$ and $\delta^{13}C$ isotope compositions of carbonates were measured with a gas ratio mass spectrometer (KIEL-III) coupled with a carbonate preparation device (Finnigan MAT 252). Powder samples were treated with phosphoric dehydrate under vacuum at 70°C. Isotope ratios were analyzed with an accuracy of ± 0.1‰ for $\delta^{18}O$ and ± 0.08‰ (1σ) for $\delta^{13}C$ and calibrated based on repeat measurements of NBS-19 and NBS-18. All oxygen and carbon isotope ratios are shown in standard notation and reported

relative to Vienna Pee Dee Belemnite (VPDB) (Supplementary Table 1) with calculated StalAge age results and host rock $\delta^{18}O$ and $\delta^{13}C$ isotope ratios.

In addition, for the Hendy Test (Table 2), carbon and oxygen isotope analyses were carried out on 10 sub-samples collected from 2 prominent layers of 27 and 103 mm from the top of the stalagmite. Microsampling was performed at ∼1 mm intervals perpendicular to the growth axis of the stalagmite. Isotope analyses were conducted using the Termofinnigan Delta PlusXP mass spectrometer at the Central Laboratory of the Middle East Technical University (METU), Türkiye.

$^{87}Sr/^{86}Sr$ isotope and trace element concentrations

Nine sub-samples (eight from the stalagmite and one from marble host rock) were selected for trace element and strontium isotope ($^{87}Sr/^{86}Sr$) analyses. Sampling was performed at the sampling locations selected for dating. Analyses were carried out at the University of Queensland using the Thermo X-series ICP-MS device for trace element analysis and Thermal Ionization Mass Spectrometer (TIMS) for the strontium isotope analysis. Detailed methodology is given in Ünal-İmer et al. (2016b).

RESULTS

Calcite textures

Different calcite textures have been identified in the YL-1 stalagmite (Fig. 4a–c). Calcite crystals exhibit an irregular structure in the interval of ca. 116.16 to ca. 116.32 ka. Polycrystals of calcite are dispersedly intertwined (Fig. 4c) along with high porosity. A more-arranged calcite fabric appears at ca. 115.49 to ca. 115.83 ka, showing a distinctive layered structure. Layers are characterized by alternations of light- and dark-colored bands. While the light-colored layers vary between ∼0.05–0.1 mm in thickness, dark-colored layers have thicknesses changing between 0.2 and 0.9 mm (Fig. 4b). A transition to a coarse-grained compact texture is observed in the layers at around 115.27 ka. Anhedral or subhedral mosaic calcite crystals have variable diameter size, ranging from ∼10 μm to 1 mm. There is no significant porosity developed between the crystals (Fig. 4a).

Table 1. MC-ICP-MS U-Series age results (ka) of the YL-1 stalagmite (Yelini Cave). Ages in bold are out of stratigraphic order and were not utilized in StalAge calculations (Scholz and Hoffmann, 2011).

Sample ID	Distance From Top (mm)	U (ppm)	^{232}Th (ppb)	$^{230}Th/^{232}Th$	$^{230}Th/^{238}U$	$^{234}U/^{238}U$	Corr. [$^{234}U/^{238}U$]	Corr. ^{230}Th age (ka)
YL-01	1	0.1748	2.213 ± 0.0036	157.5 ± 0.63	0.6570	1.0328	1.0447 ± 0.0015	109.05 ± 0.74
YL-13	**13**	**0.3167**	**0.492 ± 0.0007**	**1322.8 ± 3.4**	**0.6778**	**1.0247**	**1.0345 ± 0.0011**	**117.27 ± 0.50**
YL-25	**25**	**0.2367**	**1.322 ± 0.0017**	**376.11 ± 0.7**	**0.6925**	**1.0314**	**1.0441 ± 0.0012**	**120.17 ± 0.37**
YL-33	**33**	**0.2391**	**0.390 ± 0.0008**	**1271.0 ± 4.5**	**0.6830**	**1.0329**	**1.0457 ± 0.0016**	**117.00 ± 0.67**
YL-45	45	0.3036	0.312 ± 0.0008	2020.0 ± 7.7	0.6843	1.0377	1.0524 ± 0.0012	116.28 ± 0.63
YL-72	**72**	**0.2895**	**0.460 ± 0.0007**	**1329.4 ± 4.8**	**0.6964**	**1.0470**	**1.0655 ± 0.0014**	**117.81 ± 0.73**
YL-82	82	0.3200	0.243 ± 0.0004	2732.8 ± 6.5	0.6851	1.0364	1.0507 ± 0.0014	116.82 ± 0.43
YL-98	98	0.2871	0.247 ± 0.0004	2441.3 ± 7.3	0.6911	1.0447	1.0622 ± 0.0016	116.76 ± 0.60
YL-112	112	0.3015	0.259 ± 0.0006	2437.4 ± 9.2	0.6905	1.0440	1.0611 ± 0.0010	116.72 ± 0.63
YL-131	131	0.3953	1.636 ± 0.0024	500.0 ± 1.43	0.6817	1.0302	1.0421 ± 0.0018	117.15 ± 0.60

Table 2. Results (δ^{18}O and δ^{13}C values, ‰ VPDB) of Hendy Tests.

Depth (mm)	Distance from the growth axis (mm)	δ^{18}O (‰, VPDB)	δ^{13}C (‰, VPDB)
27	4	−12.71	−9.91
27	5	−12.36	−9.70
27	6	−12.42	−9.77
27	7	−12.40	−9.75
27	8	−12.41	−9.79
103	3	−11.30	−8.50
103	4	−11.24	−8.43
103	5	−11.04	−8.50
103	6	−11.15	−8.45
103	7	−11.07	−8.43

XRD results indicate that the main mineral in the stalagmite is calcite. In addition to calcite, the results also show minor aragonite peaks. However, no residual aragonite was detected petrographically in the thin sections.

U-series dating and age–depth model

Results of U-series dating analyses of 10 samples from the YL-1 stalagmite are presented in Table 1. Accordingly, deposition of the stalagmite started at 117.15 ± 0.60 ka and stopped at 109.05 ± 0.74 ka. The analyses at depths of 13, 25, 33, and 72 mm yielded dates beyond the growth period of the stalagmite. The outlier ages may be related to the transport of clastic thorium (^{232}Th) in groundwater and its inclusion in the stalagmite (White 2004; Fairchild and Baker, 2012). Therefore, the age–depth model was constructed through the StalAge code in R (Scholz and Hoffmann, 2011; Scholz et al., 2012) using the ages (n = 6) in stratigraphic order within the margin of error (Fig. 3).

Stable isotopes

Calculated ages (ka) (StalAge results) and corresponding stable isotope values (in per mil [‰] relative to VPDB) are given in Supplementary Table 1. The δ^{18}O and δ^{13}C values of the host marble sample are 2.27‰ and −0.79‰, respectively (Supplementary Table 1). δ^{18}O values of YL-1 stalagmite calcite samples change from −12.84‰ to −10.56‰ (VPDB) with an average value of −11.63‰ (Fig. 5a). Early layers of YL-1 are represented by relatively high δ^{18}O values including the maximum measured δ^{18}O composition of −10.56‰ at 116.83 (+0.58/ −0.42) ka. Then, after a rapid negative shift, an enrichment of 1.33‰ is observed at 116.70 (+0.62/−0.35) through 116.63 (+0.46/−0.40) ka (Fig. 5a). This is followed by a decrease of 1.83‰ at 116.51 (+0.38/−0.50) ka. This period corresponds to the lowest δ^{18}O values throughout the stalagmite (−12.84‰). After this low period, a rapid enrichment of 1.88‰ occurs towards 116.24 (+0.53/−0.86) ka, and a gradual decrease is noticeable towards 115.87 (+0.83/−1.71) ka. From this point onwards, calcite deposition ceases with a gradual enrichment in isotope ratios.

The δ^{13}C values of the YL-1 stalagmite are in the range of −9.63‰ to −7.89‰ (with an average of −8.78‰, VPDB)
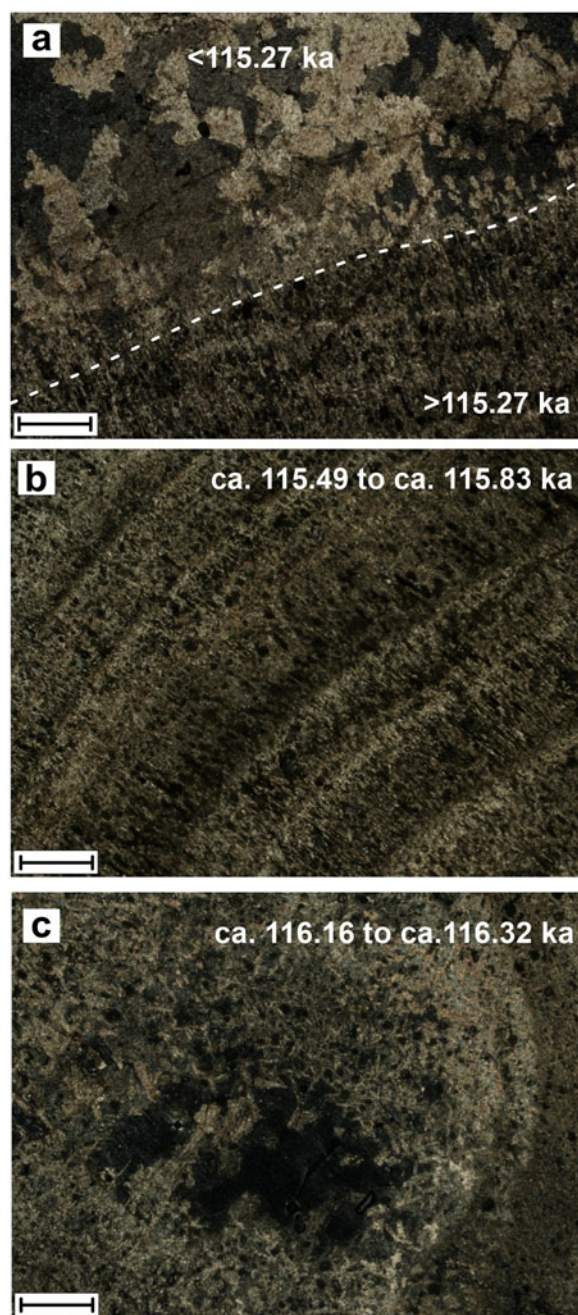

Figure 4. Thin section images of YL-1 stalagmite under crossed nicols. The scales are 500 μm. (a) Transition of fine-grained calcite crystals to mosaic calcite crystals (dashed line), (b) distinctive layered structure of fine-grained calcite, (c) irregular (or dendritic) calcite crystals.

(Fig. 5a). Variation in δ^{13}C compositions along sample YL-1 is less pronounced compared to variation in δ^{18}O ratios. Earliest stalagmite layers (at 117.05 [+0.48/−0.38] ka) are characterized by relatively enriched δ^{13}C values (−7.90‰). This is followed by a relative depletion in δ^{13}C values (−9.01‰) at 117.01 (+0.51/−0.37) ka and an enrichment of 1.01‰ at 116.65 (+0.51/−0.39) ka. Then δ^{13}C values show a negative shift after a slight enrichment in the range of 116.16 (+0.60/−1.03) to 116.07 (+0.67/−1.24) ka.

There is a weak positive correlation between the δ^{13}C and δ^{18}O values of the YL-1 stalagmite ($R^2 = 0.31$) (Fig. 5b). The sub-

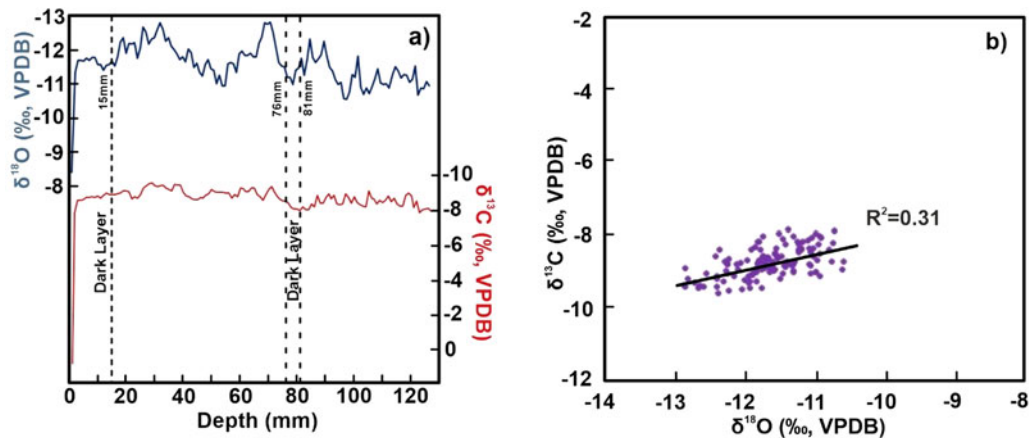**Figure 5.** (a) Diagram showing variations in $\delta^{18}O$ and $\delta^{13}C$ profiles of YL-1 stalagmite with respect to its depth. (b) Correlation between $\delta^{18}O$ and $\delta^{13}C$ values.

sample from 1 mm (distance from top) has significantly high oxygen and carbon isotope values (−8.41‰ and 0.74‰, respectively). If the dripping is extremely slow or interrupted during the end of calcite deposition, isotopic enrichment may occur as a result of prolonged separation of CO_2 from the solution (Frisia et al., 2000), resulting from low effective infiltration inside the cave.

Hendy Tests

The kinetic fractionation in stalagmites may mislead the paleoclimate data obtained from the calcite (Hendy, 1971). This causes the light isotopes to be preferentially separated from the solution and concomitant enrichment of heavy isotopes in the stalagmite. For this reason, we applied the Hendy Test (Hendy, 1971) to the YL-1 stalagmite. According to the Isotopic Equilibrium Test study, the change in $\delta^{18}O$ values along a single lamina is expected not to exceed 0.5‰ (Hendy 1971; Ünal-İmer et al., 2020). $\delta^{18}O$ values of YL-1 stalagmite do not show such a variation (Table 2; Fig. 6). In addition, farther from the axis there are no reciprocal changes between $\delta^{13}C$ and $\delta^{18}O$ that indicate kinetic fractionation (Fig. 6). Therefore, it is suggested that CO_2 separation from dripping water was slow during stalagmite formation (Ünal-İmer et al., 2020) and isotopic equilibrium conditions were maintained.

How effectively the Hendy Test applications in stalagmites reflect the isotopic equilibrium is still controversial since the thickness of stalagmite layers at the growth center and edges may vary. Different kinetic fractionation effects may occur in the same layer along with possible problems with the sampling (Dorale and Liu, 2009). In addition, it is not possible to establish a precise oxygen isotope equilibrium between calcite and dripping water (McDermott et al., 2006). The Hendy Test is widely used to investigate such kinetic effects, although it does not give as precise results as the comparative isotope records from different stalagmites (Dorale and Liu, 2009).

$^{87}Sr/^{86}Sr$ and trace element compositions

$^{87}Sr/^{86}Sr$ ratios of YL-1 stalagmite vary in a narrow range from 0.707946 to 0.707987 (Table 3). These values are very close to the Sr isotope ratio of the host rock (0.707851), indicating a close genetic link between the marble host rock and the YL-1 stalagmite. The highest and lowest $^{87}Sr/^{86}Sr$ ratios in stalagmite are recorded at 71 mm and 82 mm (at the beginning of a dark layer), respectively.

Magnesium concentrations of the YL-1 stalagmite range between 764.4 ppm and 614.2 ppm (Table 3). Lowest Mg concentrations were observed at layers of 112 mm and 98 mm, whereas highest concentrations were recorded at 82 mm and 33 mm. Sr concentrations, ranging 88.9–110.6 ppm, are lower than Mg. The lowest and highest Sr contents are recorded in laminae at 82–33 mm and 13–25 mm, respectively (Table 3). Mg/Ca and Sr/Ca ratios are only weakly correlated ($R^2 = 0.15$; Fig. 7a). Phosphorus contents are 50.3–119.8 ppm, and the lowest and highest P concentrations were observed at 82 and 25 mm, respectively. Lower Cu concentrations ranging from 1.8 to 4.6 ppm have a strong positive correlation with P ($R^2 = 0.75$) (Fig. 7b). Additionally, Y (2–6 ppb), Be (12–43 ppb), and Zr (49–96 ppb) concentrations are very low. Beryllium and Phosphorus are positively correlated ($R^2 = 0.73$), whereas P weakly relates with Y and Zr ($R^2 = 0.12$ and $R^2 = 0.18$, respectively; Fig. 7c).

DISCUSSION

Speleothem growth and deposition rate

Speleothem formation is an important indicator of climatic conditions since the growth of speleothem depends crucially on water availability (Genty et al., 2006). Although growth rate is an
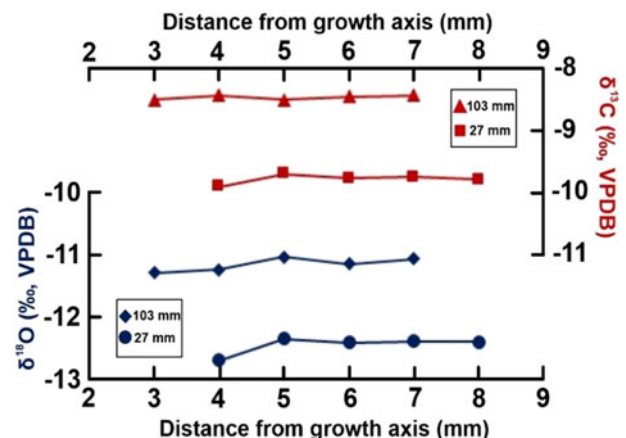

Figure 6. Hendy Test plots for the $\delta^{18}O$ and $\delta^{13}C$ analyses performed on laminae at 27 and 103 mm of YL-1.

Table 3. ICP-MS trace elements concentrations and TIMS $^{87}Sr/^{86}Sr$ ratios of the YL-1 stalagmite and marble host rock.

Depth (mm)	Age (ka)	Ca (ppm)	Mg (ppm)	Sr (ppm)	P (ppm)	Cu (ppm)	Y (ppb)	Be (ppb)	Zr (ppb)	$^{87}Sr/^{86}Sr$
13	115.19	342975	719.6	88.9	81.3	3	2	20	56	0.707956
25	115.68	347472	669.4	93.3	119.8	4	4	32	74	0.707958
33	115.89	351267	764.4	103.4	113.4	4.6	3	43	85	0.707966
45	116.08	352120	750.2	99.8	88.9	4.3	6	20	79	0.707978
71	116.51	359815	684.6	96.2	88.6	3.9	5	31	69	0.707987
82	116.67	365554	763.1	110.6	50.3	1.8	2	12	49	0.707946
98	116.83	364405	614.2	102.8	70.0	2.4	4	17	96	0.707985
112	116.94	357961	622.6	94.6	75.4	2.4	2	26	69	0.707968
Marble host rock	—	370549	1716.5	142.1	27.1	—	63	4	5	0.707851

important proxy, growth mainly responds to changes in temperature, precipitation, and soil activities (Kaufmann and Dreybrodt, 2004). Sufficient Ca^{2+} dissolution from the marble wall-rock and the amount of CO_2 in the soil, which controls the solution acidity, are closely correlated with the extent of calcite precipitation in speleothems (Kaufmann, 2003; Vansteenberge et al., 2019). In addition, water loss through evaporation in the unsaturated region, evapotranspiration, and surface flow also can reduce the effect of dripping water (Vaks et al., 2003). Therefore, lowering of the P/E ratio may cause a decrease in growth rate of speleothems or even hiatuses in speleothem growth. Speleothem growth occurs under humid climatic conditions (Genty et al., 2006; Fairchild and Baker, 2012). Based on the age–depth model, the YL-1 stalagmite was deposited at 117.13 (+0.57/−0.44) to 114.87 (+1.63/−2.89) ka and is characterized dominantly by thin layers of fine-grained calcite (Fig. 4).

The growth rate of YL-1 is found to be ~0.10 mm/yr from the beginning towards ca. 116.94 ka (Fig. 8). After this period, the deposition rate increased to 0.12 mm/yr and slightly dropped to 0.10 mm/year at ca. 116.83 ka. The first notable decrease in growth rate to 0.63 mm/yr is seen at ca. 116.67 ka, which corresponds to the beginning of the detrital-rich brown layer at ca. 116.67 ka (77–80 mm depth; Fig. 3). Age results, however, suggest that the hiatus here was not prolonged. A second noticeable growth rate decrease, down to 0.04 mm/yr, appears at ca. 116.08 ka where the calcite fabric displays interrupted crystallization and dendritic-type porous fabric (Figs. 4 and 8). Generally slow growth rate throughout the YL-1 deposition and even slower growth rates in the upper 1 ka section are linked to the lowering P/E (precipitation/evaporation) ratio in the cave. The onset of stalagmite deposition coincides with the GS 26 cold phase represented in the Greenland ice core records (NGRIP members, 2004). This indicates the presence of a positive moisture balance in the region during the cold phase, which is not surprising considering the semi-arid climatic conditions of the central Anatolian region. Under current climatic conditions, a relatively low annual precipitation rate of 300–500 mm/yr and average summer temperatures reaching 23°C cause sub-cloud and/or surface evaporation in the region (Schemmel et al., 2013). Therefore, "effective moisture" (precipitation−evaporation) controlling speleothem growth is of great importance (Hodge et al., 2008). Increased overall precipitation and lower temperatures in the region indicate higher "effective precipitation" or positive P−E.

$\delta^{18}O$ and $\delta^{13}C$ variations

In order to define the mechanisms controlling changes in $\delta^{18}O_{cc}$, it is important to outline controls on the $\delta^{18}O_{water}$ in that region. There are a number of "isotopic effects" that cause variations in $\delta^{18}O_{water}$, including the amount of precipitation, latitude differences, ice volume changes, seasonal changes, temperature, and changes in moisture source (Lachniet, 2009). In addition, other factors such as evaporation at the surface and in the epikarst region, water residence time in the karstic zone, groundwater mixing, and calcite precipitation rate provide important controls on $\delta^{18}O_{cc}$ (McDermott et al., 2006; Rowe et al., 2012). Hence, the factors acting on $\delta^{18}O_{cc}$ represent a complex system (Lachniet, 2009; Rowe et al., 2012).

At Yelini, the rock column (marble/recrystallized limestone) above the cave has low thickness (5 m at most) (Nazik et al., 2001). This might have reduced the possibility of mixing of dripping water with groundwater having different isotopic signatures due to lower residence times (Lachniet, 2009). Therefore, it is thought that atmospheric processes exerted a major control on $\delta^{18}O_{cc}$.

Previous studies on speleothem $\delta^{18}O_{cc}$ in the Mediterranean region examined the "amount effect," which is based on the inverse correlation between rainfall amount and $\delta^{18}O_{ppt}$, the "source effect" focusing on Atlantic- vs. Mediterranean-sourced humidity that varies during stadial and interstadial transitions, and the "temperature effect" explaining the altitude-based inverse correlation between cold conditions and $\delta^{18}O_{water}$ (Bar-Matthews et al., 1999; Jex et al., 2010; Boch et al., 2011; Rowe et al., 2012; Dumitru et al., 2018; Columbu et al., 2019). In addition to these mechanisms, there are also some studies in Türkiye that have reported a negative correlation between effective winter rainfall and $\delta^{18}O_{water}$. The speleothem record of Akçakale Cave in NE Türkiye showed a strong and consistent correlation between the October–January rainfall records and $\delta^{18}O_{cc}$ values (Jex et al., 2010), which is attributed to recharge of the karst aquifer by the autumn–winter precipitation with depleted $\delta^{18}O_{water}$ values. The isotope data of dripping waters, local springs, and streams around the Karaca Cave, which is located in southern Türkiye, also display a strong linkage with contribution from winter rainfall (Rowe et al., 2012). However, in both of these examples, the overburden above the cave is thick with high rainfall amounts during the winter, allowing for longer residence time for infiltrated water, which is less exposed to evaporation and water mixture inside the epikarst. Therefore, the P−E balance is more
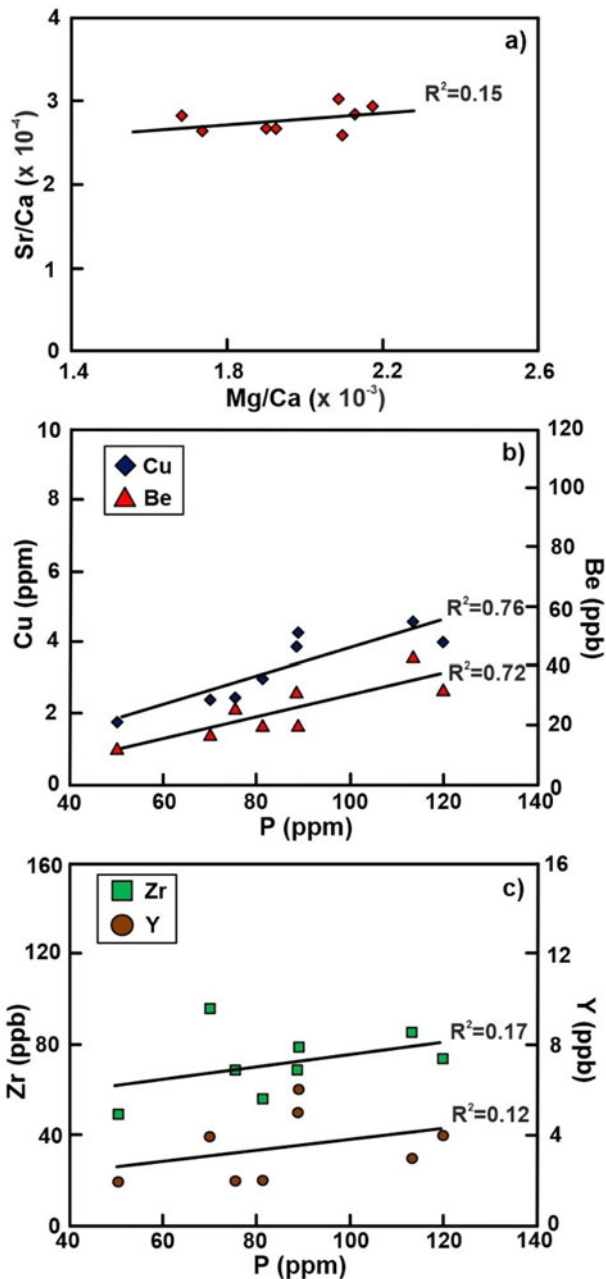
Figure 7. (a) Weak positive correlation between Sr/Ca and Mg/Ca. (b) Moderate positive correlation of Cu and Be concentrations with P concentration. (c) Weak positive correlation of Zr and Y concentrations with P concentration.

Figure 8. Temporal variations of $\delta^{18}O$, $\delta^{13}C$, $^{87}Sr/^{86}Sr$, Mg/Ca, Sr/Ca, P (ppm), Cu (ppm), Be (ppb), Y (ppb), Zr (ppb), and growth rate (mm/yr) of the YL-1 stalagmite. The anomalies in all proxies between 116.67 (+0.54/−0.38) ka and 116.65 (+0.51/−0.39) ka are noted (green vertical bar). $\delta^{18}O$ at 116.24 (+0.58/−0.86) ka (MIS 5e/5d transition) increases by 1.79‰ (yellow vertical bar). $\delta^{13}C$ values record this transition at 116.07 (+0.67/−1.24) ka as a weaker anomaly (yellow vertical bar). The decrease in growth rate is also noticeable during this period.

biased towards winter season, allowing a negative correlation with $\delta^{18}O_{cc}$. In the case of Yelini Cave, the evaporation component in the P−E balance might be important due to atmospheric circulation at the geographical location of the studied cave. The barrier effect of the mountain ranges in the northern and southern parts of Türkiye prevents moisture from moving inland (Erkan et al., 2021), resulting in a prevalence of semi-arid climatic conditions around Yelini Cave.

In arid and semi-arid areas, near-surface evaporation processes are reflected as seasonal variations in $\delta^{18}O$ (McDermott et al., 2006, and references therein). Schemmel et al. (2013) reported a modern meteoric water study suggesting that the general trend of increase in δD and $\delta^{18}O$ from the sheltered sides of the
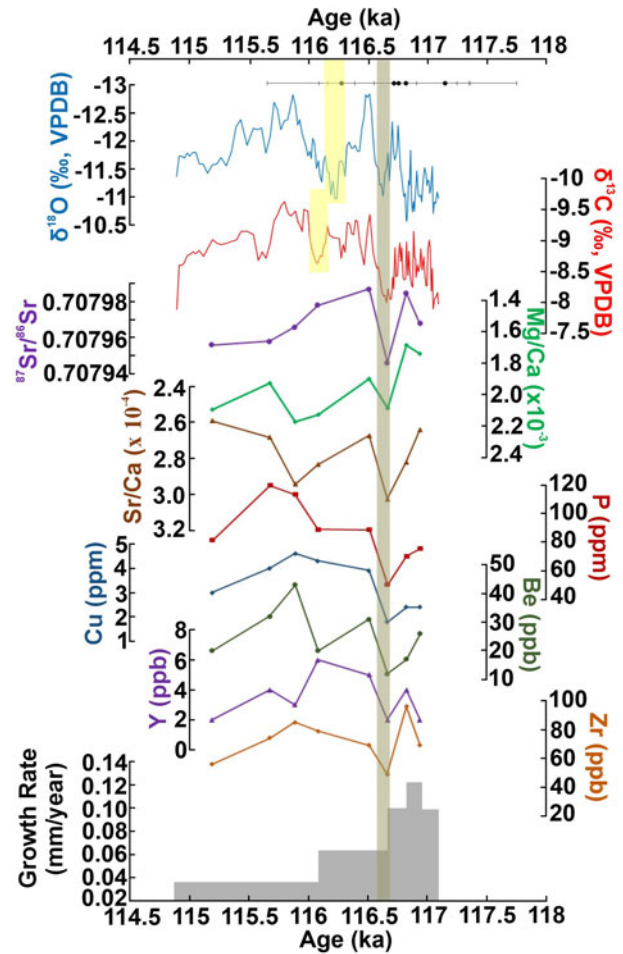
mountain ranges in the southern and northern parts of Türkiye to the interior Central Anatolian Plateau (CAP) is the result of increased sub-cloud and surface evaporation due to drought conditions. Increased evaporation conditions significantly reduce effective precipitation (P–E) in the region. This also indicates significant seasonal changes on $\delta^{18}O_{water}$ values. The $\delta^{18}O$ rainfall data for the years between 2012 and 2016 taken from the Turkish State Meteorological Service (MGM) Ankara station, which is the closest meteorological station to Yelini Cave, indicate that winter precipitation is represented by more-negative $\delta^{18}O$ values compared to other months (Dilaver et al., 2018). Similarly, stable water isotope data from CAP (Ankara) and Global Network of Isotopes in Precipitation (GNIP) Ankara station data suggest a strongly seasonal (winter dominant) rainfall pattern along the CAP (Schemmel et al., 2013). This is explained by a positive precipitation–evaporation balance during the cold season and winter-dominated groundwater recharge. Consequently, increased or decreased intensity of winter precipitation is the most likely mechanism reflecting the changes in $\delta^{18}O_{cc}$ values of the YL-1 stalagmite (Fig. 8). Lower $\delta^{18}O_{cc}$ values of the YL-1 stalagmite are attributed to the increased effect of net

effective winter precipitation and higher $\delta^{18}O_{cc}$ values are due to decreasing net effective precipitation arising from the increase in atmospheric evaporation. Adding to this is the plausible evaporation within the epikarst of Yelini Cave, due to the location of the cave close to the surface.

Changes in speleothem $\delta^{13}C_{cc}$ are directly associated with variations in isotopic contributions of carbon reservoirs including soil and atmospheric CO_2 as well as the carbonate host rock (McDermott et al., 2006; Dumitru et al., 2018). $\delta^{13}C$ values are affected by fluctuations in isotopically light soil CO_2 (Hodge et al., 2008), therefore, speleothem $\delta^{13}C_{cc}$ values strongly depend on carbon isotope composition of vegetation (C$_3$ and C$_4$ plants) growing above the cave (McDermott et al., 2006). Changes in $\delta^{13}C_{cc}$ values also may be affected by several factors that include stalactite–stalagmite fractionation (evaporation and CO_2 degassing), CO_2 gas loss of groundwater in the aquifer zone, and short water-residence times in the soil (i.e., inability to establish an equilibrium between soil water and soil CO_2) (Baker et al., 1997).

Biogenic CO_2 increase due to increase in rainfall during hot and humid periods has a negative-trending effect on $\delta^{13}C_{cc}$ (Genty et al., 2003). C$_4$-type plants reflecting arid environments and C$_3$-type plants reflecting humid environments cause different $\delta^{13}C$ values in speleothems depending on the climate ($\delta^{13}C$ for C$_4$ and C$_3$ plants are −6 to +2‰ and −14 to −6‰, respectively) (McDermott et al., 2006). On the other hand, decreasing CO_2 contribution of biogenic carbon during cold and dry periods, increasing dissolved carbon content, PCP, primary carbonate host rock, and atmospheric dissolved carbon concentrations result in high $\delta^{13}C_{cc}$ values in speleothems (Baker et al., 1997; Genty et al., 2006; Dumitru et al., 2018). In general, the $\delta^{13}C$ values of a speleothem are products of this equilibrium. In the YL-1 stalagmite, $\delta^{13}C$ values varying from −14 to−6‰ indicate C$_3$-type vegetation (McDermott et al., 2006) similar to the other cave records from Anatolia (e.g., Ünal-İmer et al., 2015). Modern vegetation is quite scarce at the studied cave site, but the $\delta^{13}C$ profile of the YL-1 stalagmite is associated with changes in effective winter precipitation (precipitation−evaporation). The changes towards more negative values can be explained by rises in net effective precipitation and growing seasonal moisture in the soil and carbonate rock/atmospheric components during dry seasons (Fig. 8).

$^{87}Sr/^{86}Sr$ ratios

Sr isotope values ($^{87}Sr/^{86}Sr$) measured in speleothems reflect the relative contributions of Sr dissolved from the marble host rock and exogenic Sr accumulating in the soil (Goede et al., 1998; Bar-Matthews et al., 1999; Frumkin and Stein, 2004; Li et al., 2005). The negligible extent of isotopic fractionation of $^{87}Sr/^{86}Sr$ during calcite formation enables assessment of environmental factors affecting the $^{87}Sr/^{86}Sr$ values of dripping water in a cave (Goede et al., 1998). In addition to the Sr isotope composition of the host rock, different radiogenic Sr sources (e.g., dust transport, marine salts, volcanic activity) are reflected in the $^{87}Sr/^{86}Sr$ values of the speleothems (Banner et al., 1996; Goede et al., 1998; Bar-Matthews et al., 1999; Verheyden et al., 2000; Frumkin and Stein, 2004; Li et al., 2005). This provides insights into the origin of radiogenic Sr, the effect of varying climatic conditions, and changes in the karst.

Previous studies have shown that weathering of dolomitic host rock with an increase in precipitation might cause low $^{87}Sr/^{86}Sr$ values in speleothems (Ayalon et al., 1999). Verheyden et al.

(2000) reported the dominant effect of low $^{87}Sr/^{86}Sr$ bedrock end-members and the effect of high $^{87}Sr/^{86}Sr$ clastic-phase endmembers with their time-dependent contributions. In addition to the dominant host rock contribution represented by low $^{87}Sr/^{86}Sr$ values during humid periods, terrestrial dust can cause high $^{87}Sr/^{86}Sr$ ratios in speleothems (Frumkin and Stein, 2004). The dissolution of silica-rich metamorphic rocks (as cave basement) or quartzo-feldspathic clastics in bedrock also may cause high $^{87}Sr/^{86}Sr$ in speleothems (Ünal-İmer et al., 2016a; Carolin et al., 2019). $^{87}Sr/^{86}Sr$ ratios of the YL-1 stalagmite mostly indicate genetic signatures that are similar to the host carbonate rock (0.707851) (Fig. 9). Therefore, the contribution of terrestrial dust (0.7082–0.7086; Frumkin and Stein, 2004) input (from the Sahara Desert) is thought to be limited (Ünal-İmer et al., 2016a).

$^{87}Sr/^{86}Sr$ ratios increase from 0.707968 to 0.707985 in the period of 116.94 (+0.49/−0.35) ka to 116.83 (+0.58/−0.42) ka in the YL-1 stalagmite (Fig. 9). A decrease is observed at 116.67 (+0.54/−0.38) ka to the value of 0.707946, which is concurrent with enrichments in the $\delta^{18}O$ and $\delta^{13}C$ records (Fig. 8). $^{87}Sr/^{86}Sr$ values initially show a similar increasing trend with $\delta^{18}O$; however, they then follow a different pattern at 116.67 (+0.54/−0.38) ka (Fig. 8). This difference between O–C systematics and $^{87}Sr/^{86}Sr$ ratios is likely due to the thin soil cover above the cave, increased groundwater residence time, and increase in the extent of water–host rock interaction possibly due to the decrease in groundwater recharge (Rowe et al., 2020). Lowered levels of $^{87}Sr/^{86}Sr$ at 116.67 (+0.54/−0.38) ka can be attributed to the negative P/E balance due to the decrease in winter precipitation (Fig. 9). This indicates higher contributions from the marble host rock as the water–rock interaction intensified. $^{87}Sr/^{86}Sr$ ratio rises to 0.707987 at 116.51 (+0.38/−0.50) ka, which might reflect rapid return to wetter conditions after drought (Fig. 9).

Trace element concentrations

Variations in trace element compositions of speleothems result from changes in environmental conditions, which include chemical composition of the dripping water, the amount of precipitation, the types of elements in the soil, water–rock interaction, chemical interactions during the entrance of water to the cave, and trace element exchange reactions during calcite deposition (White, 2004). Water with a certain P_{CO2} leaking from the soil zone dissolves calcium carbonate until it attains equilibrium, and absorbs trace elements (White, 2004). Some elements react rapidly with the infiltrated water while others are leached by slowly flowing seepage waters (Fairchild and Treble, 2009).
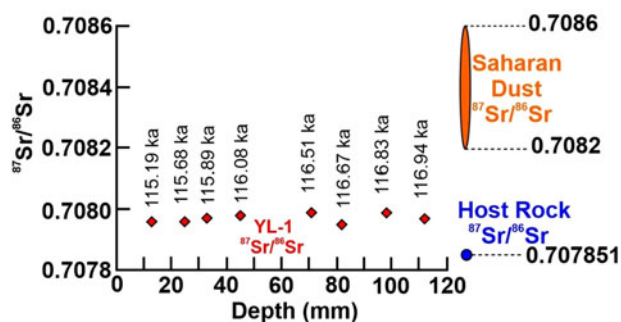

Figure 9. Graph showing the variation of $^{87}Sr/^{86}Sr$ with respect to stalagmite depth and U-series ages. $^{87}Sr/^{86}Sr$ ratios of the stalagmite indicate contribution from the marble host rock. $^{87}Sr/^{86}Sr$ values of the Jerusalem Cave stalagmite (Frumkin and Stein, 2004) are taken as the reference for terrestrial dust from the Sahara Desert.

In the YL-1 stalagmite, both Sr/Ca and Mg/Ca ratios tend to increase from the beginning of deposition up to 116.67 (+0.54/-0.38) ka (Fig. 8), despite their low sampling resolution. Sr/Ca ratio attains its maxima at 116.67(+0.54/-0.38) ka. This might be related to the increased water residence times in the epikarst. The soil CO_2 increased by the vegetation controls the bedrock dissolution and has a significant effect on the chemical composition of the water entering the cave (Hellstrom and McCulloch, 2000). This may cause changes in the amount of calcite or dolomite dissolved, and trace element concentrations in the solution may also change accordingly (Fairchild et al., 2000).

Depending on the decrease in the amount of precipitation, residence time of water in the epikarst may increase, which is accompanied by elevated concentrations of elements such as Mg and Sr as a result of extended water–rock interaction (Fairchild et al., 2000; Hellstrom and McCulloch, 2000). However, linear relationships have been reported between Mg content and increase in the deposition temperature of speleothems (Şenoğlu, 2006; Zhou et al., 2011). Şenoğlu (2006) discussed this increase using a Holocene-aged stalagmite, also from the Yelini Cave, that is located in a semi-arid climate zone. Changes in Mg/Ca ratios in a specific period of the stalagmite are associated with dry (or humid) conditions. Because the stalagmite studied by Şenoğlu (2006) was collected close to the entrance of the cave, it probably was affected by changes in air temperature. However, the YL-1 stalagmite was sampled from the distal part of the cave from the entrance (Fig. 1b) so that it should be represented by negligible airflow (Fohlmeister et al., 2020).

Concurrent increases of $\delta^{13}C$ and Mg/Ca-Sr/Ca ratios in YL-1 at ca. 116.65 ka are attributed to the Prior Calcite Precipitation (PCP) effect during a probable drought event. In addition to the dissolution process, proportional increases in Mg/Ca and Sr/Ca may also occur due to PCP along the flow path (Fairchild et al., 2000; Fairchild and Treble, 2009). As the P_{CO_2} decreases in the aquifer zone due to drought, CO_2 is separated from the solution, which then becomes supersaturated with respect to calcite (Fairchild et al., 2000). In this case, Mg/Ca and Sr/Ca ratios may increase with the separation of calcium from the solution (Fairchild and Treble, 2009), leading to a simultaneous enrichment of Mg/Ca and Sr/Ca ratios and $\delta^{13}C$ compositions of speleothems. This is because the change in speleothem $\delta^{13}C$ values is controlled by changes in plant thickness and soil CO_2. The simultaneous increases in YL-1 Mg/Ca, Sr/Ca, and $\delta^{13}C$ at 116.67 (+0.54/−0.38) ka suggest that calcite was deposited along the flow path and PCP is the dominant mechanism, which could be considered as evidence of a decrease in soil CO_2 during that time. A subsequent negative shift in $\delta^{13}C$ at 116.51 (+0.38/−0.5) ka is also reflected in variations in Sr/Ca ratios as well as in relatively less–pronounced variations in Mg/Ca ratios (Fig. 8). This can be regarded as a transition to humid conditions during which the soil CO_2 increases, possibly due to elevated vegetation density (Fairchild and Treble, 2009).

We also examined concentrations of P, Cu, Y, Be, and Zr in the YL-1 stalagmite despite low-resolution sampling for these trace elements (Figs. 8 and 10). Studies on P indicate the existence of a linear relationship between rainfall and P concentration (Huang et al., 2001; Borsato et al., 2007). The increase in the concentrations of P, Y, and Cu in an Italian stalagmite (Grotta di Ernesto Cave, ER78 stalagmite) was explained by transport of these elements as colloidal particles from the soil zone during high water seepage in autumn (Borsato et al., 2007). P, Y, Cu, and Be concentrations in YL-1 show low values in the stadial
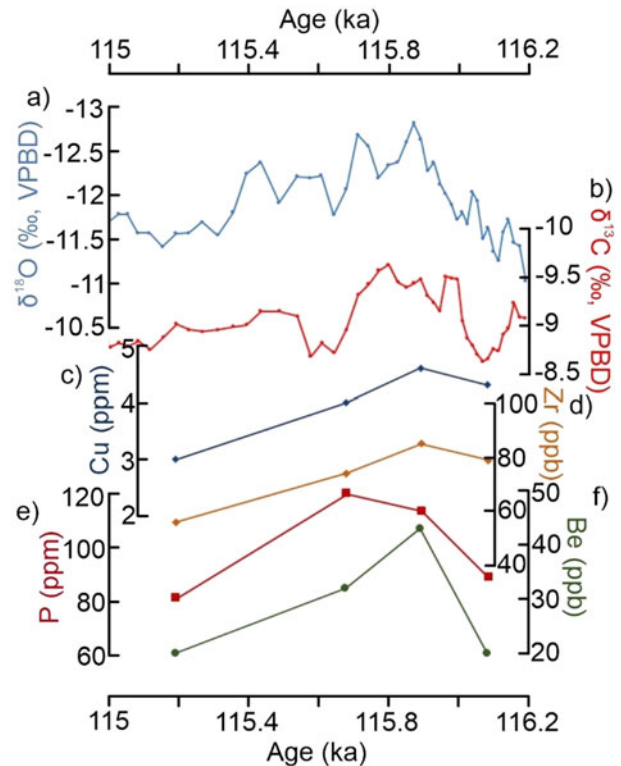

Figure 10. Temporal variations during the period 115–116.2 ka of (a) $\delta^{18}O$, (b) $\delta^{13}C$, (c) Cu (ppm), (d) Zr (ppb), (e) P (ppm), and (f) Be (ppb). Proxies display similar patterns during GI 25, which starts at 115.87 (+0.83/−1.71) ka.

period, whereas Zr contents are relatively high during the same interval (< 116.2 ka) (Fig. 8). Simultaneous decreases in P, Y, Cu, Be, and Zr at 116.67 (+0.54/−0.38) ka might be due to the decrease in the winter precipitation. During GI 25, P, Cu, Be, and Zr, as well as $\delta^{13}C$ and $\delta^{18}O$, follow a similar (contemporaneous) change (Fig. 10). Relatively high P, Y, Cu, and Be concentrations at the onset of GI 25 (115.87 ka) are associated with increased net effective precipitation and moisture availability in the soil zone (Figs. 8 and 10).

Comparison of the YL-1 stalagmite record with regional records

The climatic changes recognized in the YL-1 stalagmite record during the MIS 5e/5d transition do not match with other regional records (Fig. 11). The lack of a similar climate signal between the YL-1 stalagmite and the $\delta^{18}O$ record of the So-17A stalagmite from Sofular Cave (Badertscher et al., 2011) is due to Türkiye's northern mountains (i.e., Pontides) acting as a barrier, preventing moisture from reaching the inland regions of Türkiye via the Black Sea. This can be associated with Sofular Cave in northwestern Türkiye mainly receiving moisture from the Black Sea (Fleitmann et al., 2009; Badertscher et al., 2011). The percentages of arboreal pollen from Tenaghi–Phillippon in northern Greece (Koutsodendris et al., 2023) and from Lake Van in eastern Türkiye (Pickarski et al., 2015) also do not show a similar trend with YL-1 stalagmite profiles (Fig. 11). However, an increase in arboreal pollen percentage at 115.6 ka has been labeled as the C25 cool event in the Lake Van pollen record. This event corresponds to GS 26 in the Greenland records (NGRIP members, 2004). With uncertainties in age, a correlation can be argued

between this cold event in the Lake Van pollen record and the $\delta^{18}O$ increase at 116.2 ka in the YL-1 stalagmite (Fig. 11).

There are no clear synchronous climatic signatures between the YL-1 stalagmite and records from the Levant Basin (Fig. 11). The YL-1 stalagmite does not cover a significant part of the LIG period (130–116 ka); indeed, its growth period (117–114 ka) is considered regionally to fall into the glacial inception period (Nehme et al., 2020). However, the $\delta^{18}O$ increase at 116.2 ka in YL-1 stalagmite is synchronous with the end of MIS 5e, which is associated with the LIG. Different ages related to the last interglacial period are present in the EM records. The record from Pentadactylos Cave in Cyprus (Nehme et al., 2020) shows that the last interglacial conditions occurred between ca. 127 and ca. 123 ka, with colder and drier climate conditions prevailing during 123–110 ka (Fig. 11). A decrease in growth rate is also recorded at the end of the LIG. The end of moist conditions during the LIG period is noted at 120.3 ka in the Kanaan Cave speleothem record in Lebanon (Nehme et al., 2015), while the caves in Israel (Soreq and Peqiin) (Bar-Matthews et al., 2003; Grant et al., 2012) recorded the LIG at ca. 120 ka. Since the age interval of the YL-1 stalagmite does not reach back that far, it is not possible to compare these transitions. The isotopic changes in YL-1 during the glacial inception period (ca. 117–114 ka) also do not correspond to EM records. This discrepancy could be due to topographical effects similar to those observed in the Sofular record in the north. The southern mountain ranges (Taurides) also significantly hinder moisture transport to central Anatolia. Therefore, it is expected that the YL-1 stalagmite would show differences from records primarily reflecting eastern Mediterranean moisture. Another possibility is that these EM records may have lower resolution than the YL-1 stalagmite has during the glacial inception (ca. 114–117 ka) (Fig. 11).

Comparison of YL-1 stalagmite record – global relationships

The glacial inception period at Yelini Cave

According to the age modeling, YL-1 stalagmite growth covers the time interval of 117.13 (+0.57/−0.44) to 114.87 (+1.63/−2.89) ka, with slower growth rates after ca. 116.2 ka (Figs. 8 and 12). The onset of stalagmite formation at 117.13 (+0.57/−0.44) ka corresponds to the GS 26 period during which ice sheet growth was recorded in the Greenland ice cores (NGRIP members, 2004). As a result of reduction in insolation, a number of cooling events were reported in the North Atlantic by the end of MIS 5e during the increase of ice volume at 119–116 ka, which was recognized in the Greenland ice core records at the end of the LIG (Oppo et al., 2006; Galaasen et al., 2014; Irvali et al., 2016). An enrichment of $\delta^{18}O$ values in the YL-1 stalagmite is observed at 116.83 (+0.58/−0.42) and 116.63 (+0.46/−0.40) ka, which is close to the MIS 5e boundary. A similar enrichment trend is also noticeable for $\delta^{13}C$ at 116.65 (+0.51/−0.39) ka (Fig. 8). In addition, increases in Mg/Ca and Sr/Ca and decreases in $^{87}Sr/^{86}Sr$ ratios as well as decreases in P, Y, Cu, Be, and Zr concentrations are observed at 116.67 (+0.54/−0.38) ka (Fig. 8). Further, a substantial decrease in growth rate and a significant reduction in the diameter of the stalagmite are also recorded in the same period (Fig. 3). Therefore, we argue that a multi-centennial drought event occurred in central Anatolia at 116.65 (+0.51/−0.39) ka, which is chiefly deduced from the YL-1 stalagmite $\delta^{13}C$ profile as well as the anomalies in $\delta^{18}O$ and Sr-trace element data (Fig. 8).

The proposed drought at 116.65 (+0.51/−0.39) ka correlates well with the Eirik Drift MD03-2664 marine record in the Labrador Basin (Galaasen et al., 2014; Irvali et al., 2016; Fig. 12). The decrease in North Atlantic Deep Water (NADW) $\delta^{13}C$ values of *Cibicidoides wuellerstorfi* (an epibenthic foraminifera species; Galaasen et al., 2014) at ca. 116.8 ka fits well with the YL-1 isotopic anomalies (Fig. 12d). Similarly, in the same core, Ice Rafted Debris (IRD) and benthic foraminiferal records (e.g., $\delta^{18}O$ of *Neogloboquadrina pachyderma* and *Neogloboquadrina pachyderma* %) indicate significant cooling (Irvali et al., 2016) (Fig. 12b, c). The abundance of IRD that starts to increase at ca. 117.1 ka reaches 29% at ca. 116.9 ka, and the relative abundance of *N. pachyderma* attains 61% (Irvali et al., 2016) (Fig. 12). Massive iceberg discharge and cold-water invasion that are reported at ca. 117 ka agree well with isotopic changes in the YL-1 stalagmite (Irvali et al., 2016). Such reductions in NADW formation and subsequent weakening of the Atlantic Meridional Overturning Circulation (AMOC) caused the southward movement of cold polar waters in the Northeast Atlantic region and decreases in winter cyclone activity (Vansteenberge et al., 2016; Tzedakis et al., 2018). Rowe et al. (2012) discussed the relation between AMOC and winter cyclones that transported precipitation to the Mediterranean basin during the last glacial period. Therefore, it is likely that the YL-1 record reflects a decrease in winter precipitation at 116.65 (+0.51/−0.39) ka (Fig. 12). Similar changes were observed in speleothem records in this time interval (Fig. 12). Accordingly, $\delta^{13}C$ values at ca. 117.7–117.3 ka from the Han-9 stalagmite in Han-Sur-Lesse Cave of Belgium that represent the Eemian–Weichselian Transition (EWT) show a 4‰ increase (Vansteenberge et al., 2016, 2019), which, within the margin of error, agrees with the YL-1 stalagmite isotope record (Fig. 12h). Further, decreases in summer Sea Surface Temperature (SST) are reported in the North Atlantic ODP 980 sea core between 117 and 118 ka (Oppo et al., 2006) and in the Alboran Sea ODP 976 record at ca. 118 ka (Martrat et al., 2014).

The YL-1 stalagmite record shows significant correlations with Atlantic and European records. The $\delta^{18}O$ increase in the BAR-II stalagmite record from Baradla Cave between ca. 118.5 and 117 ka is interpreted as an arid pulse (Demény et al., 2017) (Fig. 12m). This event is recognized with simultaneous increases in $\delta^{18}O$ and $\delta^{13}C$ values in the BAR-II stalagmite. This period can be compared with the high $\delta^{18}O$ values at the beginning of the YL-1 growth. In the MD01-2443 marine record obtained from the Iberian margin (Fig. 12f), a small increase in $\delta^{18}O$ values of planktonic foraminifer (*G. bulloides*) at 116.8 ka corresponds to a decrease in SST (de Abreu et al., 2005; Voelker and de Abreu, 2011) (Fig. 12g). The HÖL-10 stalagmite from Hölloch Cave (Moseley et al., 2015) records a small $\delta^{18}O$ decrease at 117.2 ka (Fig. 12l). A similar change is represented by the $\delta^{18}O$ increase in the CAM-1 stalagmite from Campanet Cave at 117 ka (Dumitru et al., 2018) (Fig. 12i).

MIS 5e/5d transition

The MIS 5e/5d transition in the YL-1 stalagmite is represented by a $\delta^{18}O$ enrichment of 1.88‰ at 116.24 (+0.53/−0.86) ka (Fig. 12a). During this transition, the $\delta^{13}C$ values show a weaker enrichment than the $\delta^{18}O$ profile (Fig. 12c). Similarly, there is no clear trend in other isotopic and elemental proxies. A change in growth rate occurs at 116.08 ka, ca. 200 years after the transition (Fig. 8). However, highly porous (or dendritic), irregularly
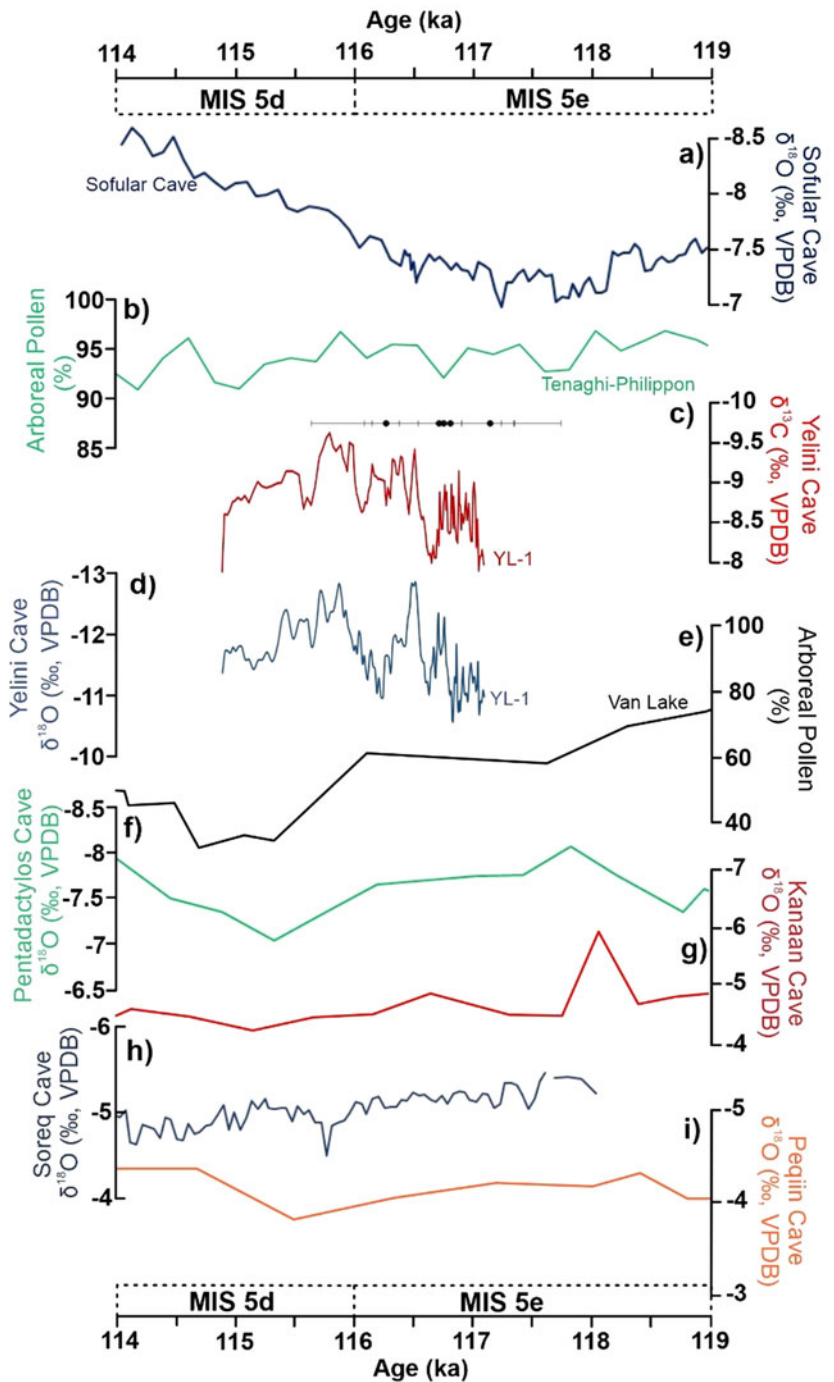
Figure 11. Comparison of the YL-1 record with regional records (from north to south). (a) Sofular Cave So-17A stalagmite $\delta^{18}O$ record (Badertscher et al., 2011); (b) Tenaghi–Phillippon cores arboreal pollen (%) record (Koutsodendris et al., 2023); (c, d) Yelini Cave YL-1 $\delta^{13}C$ and $\delta^{18}O$ stalagmite records; (e) Van Lake arboreal pollen (%) (Pickarski et al., 2015); (f) Pentadactylos Cave speleothem record (Nehme et al., 2020); (g) Kanaan Cave speleothem $\delta^{18}O$ record (Nehme et al., 2015); (h, i) Soreq and Peqiin caves $\delta^{18}O$ speleothem records (Bar-Matthews et al., 2003; Grant et al., 2012).

arranged calcite crystals during ca. 116.32–116.16 ka interval suggest irregular (non-steady) water-drip conditions coinciding with the transition (Fig. 4) (Frisia, 2015).

Elevated $\delta^{18}O$ values at 116.24 (+0.58/−0.86) ka in YL-1 coincides with the depletion of $\delta^{18}O$ at ca. 115.5 ka, representing the end of the last interglacial period in the Greenland ice record (NGRIP members, 2004) (Fig. 12h). It also matches with the upper limit of the benthic "plateau" of MIS 5e at 116.1 ± 0.9 ka (Shackleton et al., 2003). *Neogloboquadrina pachyderma* abundance reaching up to 90–95% in the eastern Nordic seas during the same time interval and the decrease in SST at the MIS 5e/5d boundary at ca. 116 ka indicate an interglacial–glacial

transition in northwest Europe (Fronval and Jansen, 1997; Knudsen et al., 2002). The pollen record of Lake Monticchio in Italy also indicates a decrease in Mediterranean woody taxa at ca.115.8 ka (Brauer et al., 2007).

The MIS 5e/5d transition is also recognized in the $\delta^{18}O$ records of the Campanet Cave CAM-1 stalagmite in Mallorca (Dumitru et al., 2018; Fig. 12i). The CAM-1 stalagmite records the MIS 5e/5d transition through increasing $\delta^{18}O$ values towards 115.4 ka. The MIS 5e/5d transition in the YL-1 stalagmite record also overlaps with the transition recognized in the Schneckenloch Cave SCH-7 (Boch et al., 2011) and the Hölloch Cave HÖL-10 stalagmites (Moseley et al., 2015) in the northern Alps (Fig. 12).
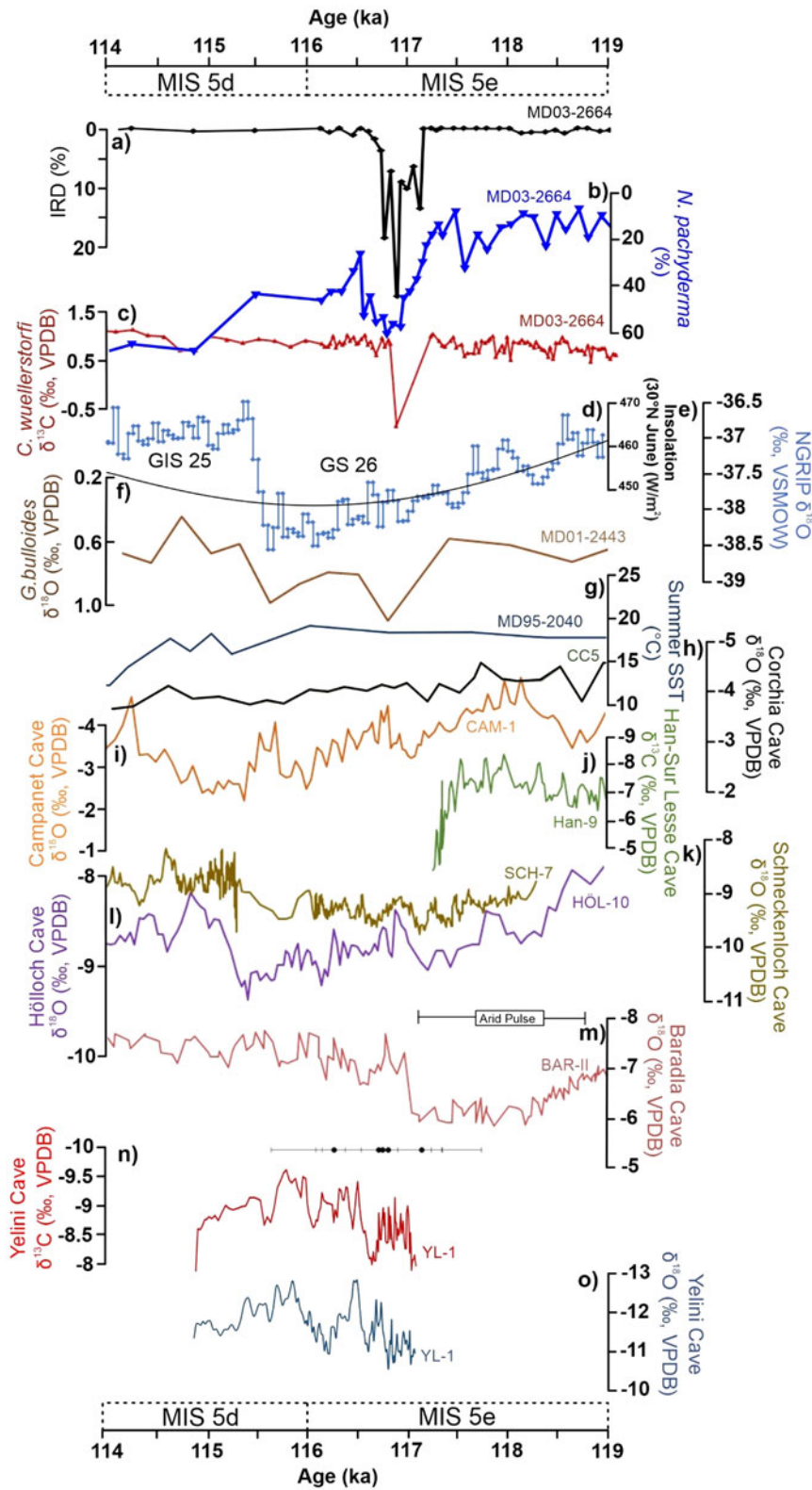
Figure 12. Comparison of the YL-1 record with global records. (a–c) MD03-2664 core records (Galaasen et al., 2014; Irvali et al., 2016), IRD (Ice-Rafted Debris), (d) 30°N June insolation curve (Berger and Loutre 1991), (e) NGRIP $\delta^{18}O$ record (NGRIP members, 2004), Vienna Standard Mean Ocean Water (VSMOW), (f) MD01-2443 planktonic foraminifera (*G. bulloides*) $\delta^{18}O$ values (de Abreu et al., 2005; Voelker and de Abreu, 2011), (g) MD95-2040 summer SST (°C) record (de Abreu et al., 2003), (h) Corchia Cave speleothem record (Drysdale et al., 2005), (i) Campanet Cave CAM-1 stalagmite $\delta^{18}O$ record (Dumitru et al., 2018), (j) Han-Sur Lesse Cave Han-9 stalagmite $\delta^{13}C$ record (Vansteenberge et al., 2016), (k) Schneckenloch Cave speleothem record (Boch et al., 2011), (l) Hölloch Cave speleothem record (Moseley et al., 2015), (m) Baradla Cave speleothem record (Demény et al., 2017), (n, o) Yelini Cave YL-1 stalagmite $\delta^{13}C$ and $\delta^{18}O$ records, respectively.

SST records from the Iberian margin MD95-2040 core do not show significant changes during the MIS 5e/5d transition and at 116.65 ka (de Abreu et al., 2003). In addition, the CC5 stalagmite record from Corchia Cave in Italy (Drysdale et al., 2005) does not provide a correlation with the YL-1 stalagmite record during this period (Fig. 12).

Large and rapid climatic improvements, in which stadial phases are temporarily interrupted by the last glacial onset (Govin et al., 2015) immediately after the MIS 5e/5d transition, are defined as Greenland Interstadial (GI) phases (Capron et al., 2010, 2012). The GI 25 transition at ca. 115.4 ka in the NGRIP record (NGRIP members, 2004) correlates with a 115.87 (+0.83/

−1.71) ka anomaly in the YL-1 record (Fig. 12h). Correlation of the Schneckenloch Cave SCH-7 and the Hölloch Cave HÖL-10 records to GI 25 at 115.3 ± 0.5 ka and 114.9 ka, respectively, are contemporaneous (within the error margin) with the YL-1 record (Fig. 12).

The YL-1 δ^{13}C profile at 115.87 (+0.83/−1.71) ka also displays a negative shift during interstadial conditions. Well-laminated, fine-grained crystals in the stalagmite after the transition may reflect regular (or near steady) dripping (and rainfall) conditions (Fig. 4). Mosaic-textured calcite, which replaces fine-grained calcite layers at ca. 115.27 ka, are concurrent with an increase in δ^{18}O profile (Figs. 4 and 5). Relatively coarser calcite crystals suggest a decrease in water availability and a decrease in the dripping regime of cave water, which in turn diminishes (or halts) stalagmite growth (Gonzalez et al., 1992; Ayalon et al., 1999).

CONCLUSIONS

This study presents a detailed investigation of the paleohydroclimatic conditions that prevailed in central Anatolia during the time period of 117.13 (+0.57/−0.44) ka to 114.87 (+1.63/−2.89) ka. δ^{18}O ratio changes recorded in the Yelini Cave YL-1 stalagmite are affected by increases or decreases in effective winter precipitation regulated by annual changes in NAO. The δ^{13}C profile of the YL-1 stalagmite reflects time-dependent changes in soil density and host rock (marble) interactions, which are controlled by variations in net effective precipitation (precipitation−evaporation) in this semi-arid region. In the YL-1 isotope record, the MIS 5e/5d boundary is marked at 116.24 (+0.53/−0.86) ka, which coincides (within the age error margin) with the MIS 5e/5d transition records in several global localities. It is also noted that the YL-1 record shows fewer correlations with regional continental records. We argue that a significant multi-centennial drought event occurred near the end of MIS 5e and ca. 400 years before the MIS 5e/5d transition in central Anatolia. This event at 116.65 (+0.51/−0.39) ka (mainly based on swings of the δ^{13}C profile) is likely due to the decrease in winter precipitation in the Anatolian Peninsula and correlates well with various global paleoclimatic archives. The YL-1 stalagmite also recorded the transition to the GI 25 wet phase at 115.87 (+0.83/−1.71) ka. As shown by trace element and stable isotope data, the transition to the GI 25 phase began with a significant increase in rainfall amount. Stalagmite growth ceased, with a gradual transition towards a colder period. The Yelini Cave YL-1 stalagmite record constitutes the first paleoclimate archive revealing the climatic conditions and timing of the MIS 5e/5d transition in central Anatolia, Türkiye.

REFERENCES

Akçar, N., Schlüchter, C., 2005. Paleoglaciations in Anatolia: a schematic review and first results. *Eiszeitalter und Gegenwart, Hannover* **55**, 102–121.

Altın, T.B., Barak, B., Altın, B.N., 2012. Change in precipitation and temperature amounts over three decades in central Anatolia, Turkey. *Atmospheric and Climate Sciences* **2**, 107–125.

Ayalon, A., Bar-Matthews, M., Kaufman, A., 1999. Petrography, strontium, barium and uranium concentrations, and strontium and uranium isotope ratios in speleothems as palaeoclimatic proxies: Soreq Cave, Israel. *The Holocene* **9**, 715–722.

Badertscher, S., Fleitmann, D., Cheng, H., Edwards, R.L., Göktürk, O.M., Zumbühl, A., Leuenberger, M., Tüysüz, O., 2011. Pleistocene water intrusions from the Mediterranean and Caspian seas into the Black Sea. *Nature Geoscience* **4**, 236–239.

Baker, A., Ito, E., Smart, P.L., McEwan, R.F., 1997. Elevated and variable values of ^{13}C in speleothems in a British cave system. *Chemical Geology* **136**, 263–270.

Banner, J.L., Musgrove, M.L., Asmerom, Y., Edwards, R.L., Hoff, J.A., 1996. High-resolution temporal record of Holocene groundwater chemistry: tracing links between climate and hydrology. *Geology* **24**, 1049–1053.

Bar-Matthews, M., Ayalon, A., Gilmour, M., Matthews, A., Hawkesworth, C.J., 2003. Sea–land oxygen isotopic relationships from planktonic foraminifera and speleothems in the Eastern Mediterranean region and their implication for paleorainfall during interglacial intervals. *Geochimica et Cosmochimica Acta* **67**, 3181–3199.

Bar-Matthews, M., Ayalon, A., Kaufman, A., Wasserburg, G.J., 1999. The Eastern Mediterranean palaeoclimate as a reflection of regional events: Soreq Cave, Israel. *Earth and Planetary Science Letters* **166**, 85–95.

Berger, A., Loutre, M.F., 1991. Insolation values for the climate of the last 10 million years. *Quaternary Science Reviews* **10**, 297–317.

Boch, R., Cheng, H., Spötl, C., Edwards, R.L., Wang, X., Häuselmann, P., 2011. NALPS: a precisely dated European climate record 120–60 ka. *Climate of the Past* **7**, 1247–1259.

Borsato, A., Frisia, S., Fairchild, I.J., Somogyi, A., Susini, J., 2007. Trace element distribution in annual stalagmite laminae mapped by micrometer-resolution X-ray fluorescence: implications for incorporation of environmentally significant species. *Geochimica et Cosmochimica Acta* **71**, 1494–1512.

Bozkurt, D., Şen, Ö.L., 2009. Precipitation in the Anatolian Peninsula: sensitivity to increased SSTs in the surrounding seas. *Climate Dynamics* **36**, 711–726.

Brauer, A., Allen, J.R.M., Mingram, J., Dulski, P., Wulf, S., Huntley, B., 2007. Evidence for last interglacial chronology and environmental change from Southern Europe. *Proceedings of the National Academy of Sciences* **104**, 450–455.

Capron, E., Landais, A., Chappellaz, J., Buiron, D., Fischer, H., Johnsen, S.J., Jouzel, J., Leuenberger, M., Masson-Delmotte, V., Stocker, T.F., 2012. A global picture of the first abrupt climatic event occurring during the last glacial inception. *Geophysical Research Letters* **39**, L15703. https://doi.org/10.1029/2012GL052656.

Capron, E., Landais, A., Chappellaz, J., Schilt, A., Buiron, D., Dahl-Jensen, D., Johnsen, S.J., *et al.*, 2010. Millennial and sub-millennial scale climatic variations recorded in polar ice cores over the last glacial period. *Climate of the Past* **6**, 345–365.

Carolin, S.A., Walker, R.T., Day, C.C., Ersek, V., Sloan, R.A., Dee, M.W., Talebian, M., Henderson, G.M., 2019. Precise timing of abrupt increase in dust activity in the Middle East coincident with 4.2 Ka social change. *Proceedings of the National Academy of Sciences* **116**, 67–72.

Chapman, M.R., Shackleton, N.J., 1999. Global ice volume fluctuations, North Atlantic ice-rafting events, and deep-ocean circulation changes between 130 and 70 ka. *Geology* **27**, 795–798.

Columbu, A., Spötl, C., Waele, J.D., Yu, T-L, Shen, C-C, Gázquez, F., 2019. A long record of MIS 7 and MIS 5 climate and environment from a western Mediterranean speleothem (SW Sardinia, Italy). *Quaternary Science Reviews* **220**, 230–243.

de Abreu, L., Shackleton, N.J., Schönfeld, J., Hall, M., Chapman, M., 2003. Millennial-scale oceanic climate variability of the Western Iberian margin during the last two glacial periods. *Marine Geology* **196**, 1–20.

de Abreu, L., Abrantes, F., Shackleton, N.J., Tzedakis, P.C., McManus, J.F., Oppo, D.W., Hall, M.A., 2005. Ocean climate variability in the eastern North Atlantic during interglacial Marine Isotope Stage 11: a partial

analogue to the Holocene? *Paleoceanography* **20**, PA3009. https://doi.org/10.1029/2004PA001091.

Demény, A., Kern, Z., Czuppon, G., Németh, A., Leél-Ossy, S., Siklósy, Z., Lin, K., *et al.*, 2017. Stable isotope compositions of speleothems from the last interglacial e Spatial patterns of climate fluctuations in Europe. *Quaternary Science Reviews* **161**, 68–80.

Demiroğlu, M., 2008. *Eskişehir–Sivrihisar–Günyüzü Havzası Hidrojeolojisi ve Hidrojeokimyası [Hydrogeology and Hydrogeochemistry of Eskişehir–Sivrihisar–Günyüzü Basin]*. PhD Thesis, Istanbul Technical University, İstanbul, Türkiye

Demiroğlu, M., Örgün, Y., 2010. Eskişehir–Sivrihisar–Günyüzü havzasının hidrojeokimyası. *The Journal of Istanbul Technical University* **9**, 3–12. [in Turkish with extended English abstract]

Dilaver, A.T., Aydın, B., Özyurt, N.N., Bayarı, C.S., 2018. *Türkiye Yağışlarının İzotop İçerikleri (2012–2016)*. DSİ-TAKK ve MGM-AD, Ankara, 44 p. [in Turkish]

Dorale, J.A., Liu, Z., 2009. Limitations of Hendy test criteria in judging the palaeoclimatic suitability of speleothems and the need for replication. *Journal of Cave and Karst Studies* **71**, 73–80.

Drysdale, R.N., Hellstrom, J.C., Zanchetta, G., Fallick, A.E., Sánchez Goñi, M.F., Couchoud, I., McDonald, J., Maas, R., Lohmann, G., Isola, I., 2009. Evidence for obliquity forcing of glacial termination II. *Science* **325**, 1527–1531.

Drysdale, R.N., Zanchetta, G., Hellstrom, J.C., Fallick, A.E., McDonald, J., Cartwright, I., 2007. Stalagmite evidence for the precise timing of North Atlantic cold events during the early last glacial. *Geology* **35**, 77–80.

Drysdale, R.N., Zanchetta, G., Hellstrom, J.C., Fallick, A.E., Zhao, J.X., 2005. Stalagmite evidence for the onset of the last interglacial in southern Europe at 129 ± 1 ka. *Geophysical Research Letters* **32**, L24708. https://doi.org/10.1029/2005GL024658.

Dumitru, O.A., Onac, B.P., Polyak, V.J., Wynn, J.G., Asmerom, Y., Fornós, J.J., 2018. Climate variability in the western Mediterranean between 121 and 67 ka derived from a Mallorcan speleothem record. *Palaeogeography, Palaeoclimatology, Palaeoecology* **506**, 128–138.

Dutton, A., Carlson, A.E., Long, A.J., Milne, G.A., Clark, P.U., DeConto, R., Horton, B.P., Rahmstorf, S., Raymo, M.E., 2015. Sea-level rise due to polar ice-sheet mass loss during past warm periods. *Science* **349**, 6244. https://doi.org/10.1126/science.aaa4019.

Erkan, G., Bayarı, S., Fleitmann D., Cheng, H., Edwards, L., Özbakır, M., 2021. Late Pleistocene–Holocene climatic implications of high-resolution stable isotope profiles of a speleothem from south-central Anatolia, Turkey. *Journal of Quaternary Science* **37**, 503–515.

Fairchild, I.J., Baker, A., 2012. *Speleothem Science: From Process to Past Environments*. John Wiley and Sons, Oxford, UK.

Fairchild, I.J., Borsato, A., Tooth, A.F., Frisia, S., Hawkesworth, C.J., Huang, Y., McDermott, F., Spiro, B., 2000. Controls on trace element (Sr-Mg) compositions of carbonate cave waters: implications for speleothem climatic records. *Chemical Geology* **166**, 255–269.

Fairchild, I.J., Treble, P.C., 2009. Trace elements in speleothems as recorders of environmental change. *Quaternary Science Reviews* **28**, 449–468.

Fleitmann, D., Cheng, H., Badertscher, S., Edwards, R.L., Mudelsee, M., Göktürk, O.M., Fankhauser, A., *et al.*, 2009. Timing and climatic impact of Greenland interstadials recorded in stalagmites from northern Turkey. *Geophysical Research Letters* **36**, L19707. https://doi.org/10.1029/2009GL040050.

Fohlmeister, J., Voarintsoa, N.R.G., Lechleitner, F.A., Boyd, M., Brandtstätter, S., Jacobson, M.J., Oster, J.L., 2020. Main controls on the stable carbon isotope composition of speleothems. *Geochimica et Cosmochimica Acta* **279**, 67–87.

Frisia, S., 2015. Microstratigraphic logging of calcite fabrics in speleothems as tool for palaeoclimate studies. *International Journal of Speleology* **44**, 1–16.

Frisia, S., Borsato, A., Fairchild, I.J., McDermott, F., 2000. Calcite fabrics, growth mechanisms and environments of formation in speleothems from the Italian Alps and southwest Ireland. *Journal of Sedimentary Research* **70**, 1183–1196.

Fronval, T., Jansen, E., 1997. Eemian and early Weichselian (140–60 ka) paleoceanography and paleoclimate in the Nordic seas with comparisons to Holocene conditions. *Paleoceanography* **12**, 443–462.

Frumkin, A., Stein, M., 2004. The Sahara–East Mediterranean dust and climate connection revealed by strontium and uranium isotopes in a Jerusalem speleothem. *Earth and Planetary Science Letters* **217**, 451–464.

Galaasen, E.V., Ninnemann, U.S., Irvali, N., Kleiven, H.F., Rosenthal, Y., Kissel, C., Hodell, D.A., 2014. Rapid reductions in North Atlantic deep water during the peak of the last interglacial period. *Science* **343**, 1129–1132.

Genty, D., Blamart, D., Ghaleb, B., Plagnes, V., Causse, C., Bakalowicz, M., Zouari, K., *et al.*, 2006. Timing and dynamics of the last deglaciation from European and North African δ^{13}C stalagmite profiles—comparison with Chinese and South Hemisphere stalagmites. *Quaternary Science Reviews* **25**, 2118–2142.

Genty, D., Blamart, D., Ouahdi, R., Gilmour, M., Baker, A., Jouzel, J., Van-Exter, S., 2003. Precise dating of Dansgaard–Oeschger climate oscillations in western Europe from stalagmite data. *Nature* **421**, 833–837.

Goede, A., McCulloch, M., McDermott, F., Hawkesworth, C., 1998. Aeolian contribution to strontium and strontium isotope variations in a Tasmanian speleothem. *Chemical Geology* **149**, 37–50.

Göktürk, O.M., Fleitmann, D., Badertscher, S., Cheng, H., Edwards R.L., Leuenberger, M., Fankhauser, A., Tüysüz, O., Kramers, J., 2011. Climate on the southern Black Sea coast during the Holocene: implications from the Sofular Cave record. *Quaternary Science Reviews* **30**, 2433–2445.

Gonzalez, L., Carpenter, S.J., Lohmann, K.C., 1992. Inorganic calcite morphology: roles of fluid chemistry and fluid flow. *Journal of Sedimentary Petrology* **62**, 382–399.

Govin, A., Capron, E., Tzedakis, P.C., Verheyden, S., Ghaleb, B., Hillaire-Marcel, C., St-Onge, G., *et al.*, 2015. Sequence of events from the onset to the demise of the last interglacial: evaluating strengths and limitations of chronologies used in climatic archives. *Quaternary Science Reviews* **129**, 1–36.

Grant, K.M., Rohling, E.J., Bar-Matthews, M., Ayalon, A., Medina-Elizalde, M., Bronk Ramsey, C., Satow, C., Roberts, A.P., 2012. Rapid coupling between ice volume and polar temperature over the past 150 kyr. *Nature* **491**, 744–747.

Hellstrom, J.C., McCulloch, M.T., 2000. Multi-proxy constraints on the climatic significance of trace element records from a New Zealand speleothem. *Earth and Planetary Science Letters* **179**, 287–297.

Hendy, C.H., 1971. The isotopic geochemistry of speleothems—I. The calculation of the effects of different modes of formation on the isotopic composition of speleothems and their applicability as palaeoclimatic indicators. *Geochimica et Cosmochimica Acta* **35**, 801–824.

Hodge, E.J., Richards, D.A., Smart, P.L., Andreo, B., Hoffmann, D.L., Mattey, D.P., González-Ramón, A., 2008. Effective precipitation in southern Spain (~266 to 46 ka) based on a speleothem stable carbon isotope record. *Quaternary Research* **69**, 447–457.

Huang, Y., Fairchild, I.J., Borsato, A., Frisia, S., Cassidy, N.J., McDermott, F., Hawkesworth, C.J., 2001. Seasonal variations in Sr, Mg and P in modern speleothems (Grotta di Ernesto, Italy). *Chemical Geology* **175**, 429–448.

Irvali, N., Ninnemann, U.S., Kleiven, H.F., Galaasen, E.V., Morley, A., Rosenthal, Y., 2016. Evidence for regional cooling, frontal advances, and East Greenland Ice Sheet changes during the demise of the last interglacial. *Quaternary Science Reviews* **150**, 184–199.

Jacobson, M.J., Flohr, P., Gascoigne, A., Leng, M.J., Sadekov, A., Cheng, H., Edwards, R.L., Tüysüz, O., Fleitmann, D., 2021. Heterogenous Late Holocene climate in the Eastern Mediterranean—the Kocain Cave record from SW Turkey. *Geophysical Research Letters* **48**, e2021GL094733. https://doi.org/10.1029/2021GL094733.

Jacobson, M.J., Pickett, J., Gascoigne, A.L., Fleitmann, D., Elton, H., 2022, settlement, environment, and climate change in SW Anatolia: dynamics of regional variation and the end of Antiquity. *PLoS ONE* **17**, e0270295. https://doi.org/10.1371/journal.pone.0270295.

Jex, C.N., Baker, A., Fairchild, I.J., Eastwood, W.J., Leng, M.J., Sloane, H.J., Thomas, L., Bekaroğlu, E., 2010. Calibration of δ^{18}O with instrumental climatic records from a modern Turkish speleothem. *Global and Planetary Change* **71**, 207–217.

Johnsen, S.J., Clausen, H.B., Dansgaard, W., Gundestrup, N.S., Hammer, C.U., Andersen, U., Andersen, K.K., *et al.*, 1997. The δ^{18}O record along the Greenland Ice Core Project deep ice core and the problem of possible

Eemian climatic instability. *Journal of Geophysical Research* **102**, 26397–26410.

Kaufmann, G., 2003. Stalagmite growth and palaeo-climate: the numerical perspective. *Earth and Planetary Science Letters* **214**, 251–266.

Kaufmann, G., Dreybrodt, W., 2004. Stalagmite growth and palaeoclimate: an inverse approach. *Earth and Planetary Science Letters* **224**, 529–545.

Knudsen, K.-L., Seidenkrantz, M.-S., Kristensen, P., 2002. Last interglacial and early glacial circulation in the northern North Atlantic Ocean. *Quaternary Research* **58**, 22–26.

Koç, K., Koşun, E., Cheng, H., Demirtaş, F., Edwards, R.L, Fleitmann, D., 2020. Black carbon traces of human activities in stalagmites from Turkey. *Journal of Archaeological Science* **123**, 105255. https://doi.org/10.1016/j.jas.2020.105255.

Koutsodendris, A., Dakos, V., Fletcher, W.J., Knipping, M., Kotthoff, U., Milner, A.M., Müller, U.C., *et al.*, 2023. Atmospheric CO_2 forcing on Mediterranean biomes during the past 500 kyrs. *Nature Communications* **14**, 1664. https://doi.org/10.1038/s41467-023-37388-x.

Kukla, G.J., Bender, M.L., de Beaulieu J.L., Bond, G., Broecker, W.S., Cleveringa, P., Gavin, J.E., *et al.*, 2002. Last interglacial climates. *Quaternary Research* **58**, 2–13.

Lachniet, M.S., 2009. Climatic and environmental controls on speleothem oxygen-isotope values. *Quaternary Science Reviews* **28**, 412–432.

Li, H.C., Ku, T.L., You, C.F., Cheng, H., Edwards, R.L., Ma, Z.B., Tsai, W.S., Li, M.D., 2005. $^{87}Sr/^{86}Sr$ and Sr/Ca in speleothems for paleoclimate reconstruction in Central China between 70 and 280 kyr ago. *Geochimica et Cosmochimica Acta* **69**, 3933–3947.

Martrat, B., Jimenez-Amat, P., Zahn, R., Grimalt, J.O., 2014. Similarities and dissimilarities between the last two deglaciations and interglaciations in the North Atlantic region. *Quaternary Science Reviews* **99**, 122–134.

McDermott, F., Schwarcz, H.P., Rowe, P.J., 2006. Isotopes in speleothems. In: Leng, M.J. (Ed.), *Isotopes in Palaeoenvironmental Research*. Springer, Dordrecht, The Netherlands, pp. 185–226.

McManus, J.F., Bond, G.C., Broecker, W.S., Johnsen, S., Labeyrie, L., Higgins, S., 1994. High-resolution climate records from the North Atlantic during the last interglacial. *Nature* **371**, 326–329.

Melki, T., Kallel, N., Fontugne, M., 2010. The nature of transitions from dry to wet condition during sapropel events in the Eastern Mediterranean Sea. *Palaeogeography, Palaeoclimatology, Palaeoecology* **291**, 267–285.

Moseley, G.E., Spötl, C., Cheng, H., Boch, R., Min, A., Edwards, R.L., 2015. Termination-II interstadial/stadial climate change recorded in two stalagmites from the north European Alps. *Quaternary Science Reviews* **127**, 229–239.

Nazik, L., Törk, K., Acar, C., Özel, E., Mengi, H., Aksoy, B., Tuncer, K., Güner, N., Ekmekçi, M., Başal, A., 2001. *Orta Sakarya Havzasının (Eskişehir ve Bilecik Doğusu) Doğal Mağaraları*. General Directorate of Mineral Research and Exploration (MTA) Report, 178 p.

Nehme, C., Kluge, T., Verheyden, S., Nader, F., Charalambidou, I., Weissbach, T., Gucel, S., *et al.*, 2020. Speleothem record from Pentadactylos Cave (Cyprus): new insights into climatic variations during MIS 6 and MIS 5 in the Eastern Mediterranean. *Quaternary Science Reviews* **250**, 106663. https://doi.org/10.1016/j.quascirev.2020.106663.

Nehme, C., Verheyden, S., Noble, S.R, Farrant, A.R., Sahy, D., Hellstrom, J., Delannoy, J.J., Claeys, P., 2015. Reconstruction of MIS 5 climate in the central Levant using a stalagmite from Kanaan Cave, Lebanon. *Climate of the Past* **11**, 1785–1799.

Nicholson, S.L., Jacobson, M.J., Hosfield, R., Fleitmann, D., 2021. The stalagmite record of southern Arabia: climatic extremes, human evolution and societal development. *Frontiers in Earth Science* **9**, 749488. https://doi.org/10.3389/feart.2021.749488.

North Greenland Ice Core Project (NGRIP) members, 2004. High-resolution record of Northern Hemisphere climate extending into the last interglacial period. *Nature* **431**, 147–151.

Oppo, D.W., Keigwin, L.D., McManus, J.F., Cullen, J.L., 2001. Persistent suborbital climate variability in Marine Isotope Stage 5 and Termination II. *Paleoceanography* **16**, 280–292.

Oppo, D.W., McManus, J.F., Cullen, J., 2006. Evolution and demise of the last interglacial warmth in the subpolar North Atlantic. *Quaternary Science Reviews* **25**, 3268–3277.

Pickarski, N., Kwiecien, O., Djamali, M., Litt, T., 2015. Vegetation and environmental changes during the last interglacial in eastern Anatolia (Turkey): a new high-resolution pollen record from Lake Van. *Palaeogeography, Palaeoclimatology, Palaeoecology* **435**, 145–158.

Rowe, P.J., Mason, J.E., Andrews, J.E., Marca, A.D., Thomas, L., van Calsteren, P., Jex, C.N., Vonhof, H.B., Al-Omari, S., 2012. Speleothem isotopic evidence of winter rainfall variability in northeast Turkey between 77 and 6 ka. *Quaternary Science Reviews* **45**, 60–72.

Rowe, P.J, Wickens, L.B., Sahy, D., Marca, A.D., Peckover, E., Noble, S., Özkul, M., Baykara, M.O., Millar, I.L., Andrews J.E., 2020. Multi-proxy speleothem record of climate instability during the early last interglacial in southern Turkey. *Palaeogeography, Palaeoclimatology, Palaeoecology* **538**, 109422. https://doi.org/10.1016/j.palaeo.2019.109422.

Sánchez Goñi, M.F., Bakker, P., Desprat, S., Carlson, A.E., Van Meerbeeck, C.J., Peyron, O., Naughton, F., *et al.*, 2012. European climate optimum and enhanced Greenland melt during the last interglacial. *Geology* **40**, 627–630.

Sánchez Goñi, M.F., Eynaud, F., Turon, J.L., Shackleton, N.J., 1999. High resolution palynological record off the Iberian margin: direct land–sea correlation for the Last Interglacial complex. *Earth and Planetary Science Letters* **171**, 123–137.

Schemmel, F., Mikes, T., Rojay, B., Mulch, A., 2013. The impact of topography on isotopes in precipitation across the central Anatolian plateau (Turkey). *American Journal of Science* **313**, 61–80.

Scholz, D., Hoffmann, D.L., 2011. StalAge – an algorithm designed for construction of speleothem age models. *Quaternary Geochronology* **6**, 369–382.

Scholz, D., Hoffmann, D.L., Hellstrom J., Ramsey C.B., 2012. A comparison of different methods for speleothem age modelling. *Quaternary Geochronology* **14**, 94–104.

Şenoğlu, G., 2006. *Mağara Çökellerinin İz Element İçeriğinden Paleoiklim Koşullarının Belirlenmesi*. MSc Thesis, Hacettepe University, Ankara, Türkiye

Shackleton, N.J., Sánchez Goñi, M.F., Pailler, D., Lancelot, Y., 2003. Marine Isotope Substage 5e and the Eemian interglacial. *Global and Planetary Change* **3**, 151–155.

Türkeş, M., 2003. Spatial and temporal variations in precipitation and aridity index series of Turkey. In: Bolle, H.J. (Ed.), *Mediterranean Climate*. Springer, Heidelberg, pp. 181–213.

Türkeş, M., 2020. Climate and drought in Turkey. In: Harmancioglu, N.B., Altinbilek, D. (Eds.), *Water Resources of Turkey, World Water Resources*. Springer, Cham, pp. 85–125.

Türkeş, M., Erlat, E., 2003. Precipitation changes and variability in Turkey linked to the North Atlantic oscillation during the period 1930–2000. *International Journal of Climatology* **23**, 1771–1796.

Türkeş, M., Erlat, E., 2005. Climatological responses of winter precipitation in Turkey to variability of the North Atlantic Oscillation during the period 1930– 2001. *Theoretical and Applied Climatology* **81**, 45–69.

Tzedakis, P.C., Drysdale, R.N., Margari, V., Skinner, L.C., Menviel, L., Rhodes, R.H., Taschetto, A.S., *et al.*, 2018. Enhanced climate instability in the North Atlantic and southern Europe during the last interglacial. *Nature Communications* **9**, 4235. https://doi.org/10.1038/s41467-018-06683-3.

Ünal, Y.S., Deniz, A., Toros, H., İncecik, S., 2012. Temporal and spatial patterns of precipitation variability for annual, wet, and dry seasons in Turkey. *International Journal Climatology* **32**, 392–405.

Ünal-İmer, E., Shulmeister, J., Zhao, J.X., Uysal, I.T., Feng, Y.X., Duc Nguyen, A., Yüce, G., 2015. An 80 kyr-long continuous speleothem record from Dim Cave, SW Turkey with paleoclimatic implications for the eastern Mediterranean. *Scientific Reports* **5**, 13560. https://doi.org/10.1038/srep13560.

Ünal-İmer, E., Shulmeister, J., Zhao, J.X., Uysal, I.T., and Feng, Y.X., 2016a. High-resolution trace element and stable/radiogenic isotope profiles of late Pleistocene to Holocene speleothems from Dim Cave, SW Turkey. *Palaeogeography, Palaeoclimatology, Palaeoecology* **452**, 68–79.

Ünal-İmer, E., Uysal, I.T, Zhao, J.X., Işık, V., Shulmeister, J., İmer, A., Feng, Y.X., 2016b. CO_2 outburst events in relation to seismicity: constraints from microscale geochronology, geochemistry of Late Quaternary vein carbonates, SW Turkey. *Geochimica et Cosmochimica Acta* **187**, 21–40.

Ünal-İmer, E., Uysal, I.T., St Pierre, E., Zhao, J.X., Shulmeister, J., 2020. Last glacial climate oscillations and sudden environmental changes investigated in stalagmites from southwest Sulawesi, western Pacific. *Turkish Journal of Earth Sciences* 29, 221–241.

Vaks, A., Bar-Matthews, M., Ayalon, A., Schilman, B., Gilmour, M., Hawkesworth, C.J., Frumkin, A., Kaufman, A., Matthews, A., 2003. Paleoclimate reconstruction based on the timing of speleothem growth and oxygen and carbon isotope composition in a cave located in the rain shadow in Israel. *Quaternary Research* 59, 182–193.

Vansteenberge, S., Verheyden, S., Cheng, H., Edwards, R.L., Keppens, E., Claeys, P., 2016. Paleoclimate in continental northwestern Europe during the Eemian and early Weichselian (125–97 ka): insights from a Belgian speleothem. *Climate of the Past* 12, 1445–1458.

Vansteenberge, S., Verheyden, S., Genty, D., Blamart, D., Goderis, S., Van Malderen, S.J.M., Vanhaecke, F., et al., 2019. Characterizing the Eemian–Weichselian transition in northwestern Europe with three multiproxy speleothem archives from the Belgian Han-sur-Lesse and Remouchamps cave systems. *Quaternary Science Reviews* 208, 21–37.

Verheyden, S., Keppens, E., Fairchild, I.J., McDermott, F., Weis, D., 2000. Mg, Sr and Sr isotope geochemistry of a Belgian Holocene speleothem: implications for paleoclimate reconstructions. *Chemical Geology* 169, 131–14.

Voelker, A.H.L., de Abreu L., 2011. A review of abrupt climate change events in the northeastern Atlantic Ocean (Iberian margin): latitudinal, longitudinal, and vertical gradients. In: Rashid H., Polyak L., Mosley-Thompson E. (Eds.), *Abrupt Climate Change: Mechanisms, Patterns, and Impacts*. Geophysical Monograph Series 193, pp. 15–37.

White, W.B., 2004. Palaeoclimate records from speleothems in limestone caves. In: Sasowsky, I.D., Mylroie, J. (Eds.), *Studies of Cave Sediments. Physical and Chemical Records of Palaeoclimate*. Kluwer Academic, New York, pp. 135–175.

Zhao, J.X., Hu, K., Collerson, K.D., Xu, H.K., 2001. Thermal ionization mass spectrometry U-series dating of a hominid site near Nanjing, China. *Geology* 29, 27–30.

Zhou, H.Y., Wang, Y., Huang, L.Y., Mai, S.Q., 2011. Speleothem Mg, Sr and Ba records during the MIS 5c–d, and implications for paleoclimate change in NE Sichuan, Central China. *Chinese Science Bulletin* 56, 3445–3450.